Radiation-Induced Metabolic Reprogramming of Fibroblasts Regulates the Breast Cancer Microenvironment

Kevin C. Corn[1], Lucy S. Britto[2], Youssef K. Mohamed[1], Yoanna I. Ivanova[2], Tian Zhu[1], and Marjan Rafat[1,2,3,*]

[1]Department of Chemical and Biomolecular Engineering, Vanderbilt University, Nashville, TN, USA

[2]Department of Biomedical Engineering, Vanderbilt University, Nashville, TN, USA

[3]Department of Radiation Oncology, Vanderbilt University Medical Center, Nashville, TN, USA

*Author for correspondence: Marjan Rafat, Engineering and Science Building, Rm. 426, Vanderbilt University, Nashville, TN 37212. Phone: (615) 343-3389, Fax: (615) 343-7951, E-mail: marjan.rafat@vanderbilt.edu

Summary

Although radioresistant and circulating tumor cell survival has been attributed to altered metabolism, the metabolic impact of radiation therapy on stromal cells is unknown. The authors provide a burgeoning mechanism for radiation-induced metabolic crosstalk between fibroblasts and breast cancer cells that may influence recurrence.

Abstract

Patients with triple negative breast cancer (TNBC) continue to have high recurrence rates despite current interventions, including radiation therapy (RT). Radiation-resistant TNBC cells and circulating tumor cells thought to be involved in recurrence survive due to changes in their metabolic profiles, which may be influenced by their interactions with radiation-damaged stromal cells, such as fibroblasts, following treatment. How fibroblasts metabolically respond to RT and influence the metabolism of TNBC cells is poorly understood. In this study, we identify that radiation-damaged fibroblasts accumulate lipids due to increased autophagic flux. The radiation damage response allows fibroblasts to maintain increased fatty acid oxidation, overall mitochondrial respiration, and aerobic glycolysis rates, leading to increased lactate secretion. TNBC cells respond to these metabolic changes by increasing migration rates and tumor spheroid growth. Our work reveals how metabolic crosstalk between irradiated fibroblasts and TNBC cells leads to a microenvironment conducive to recurrence.

Graphical Abstract

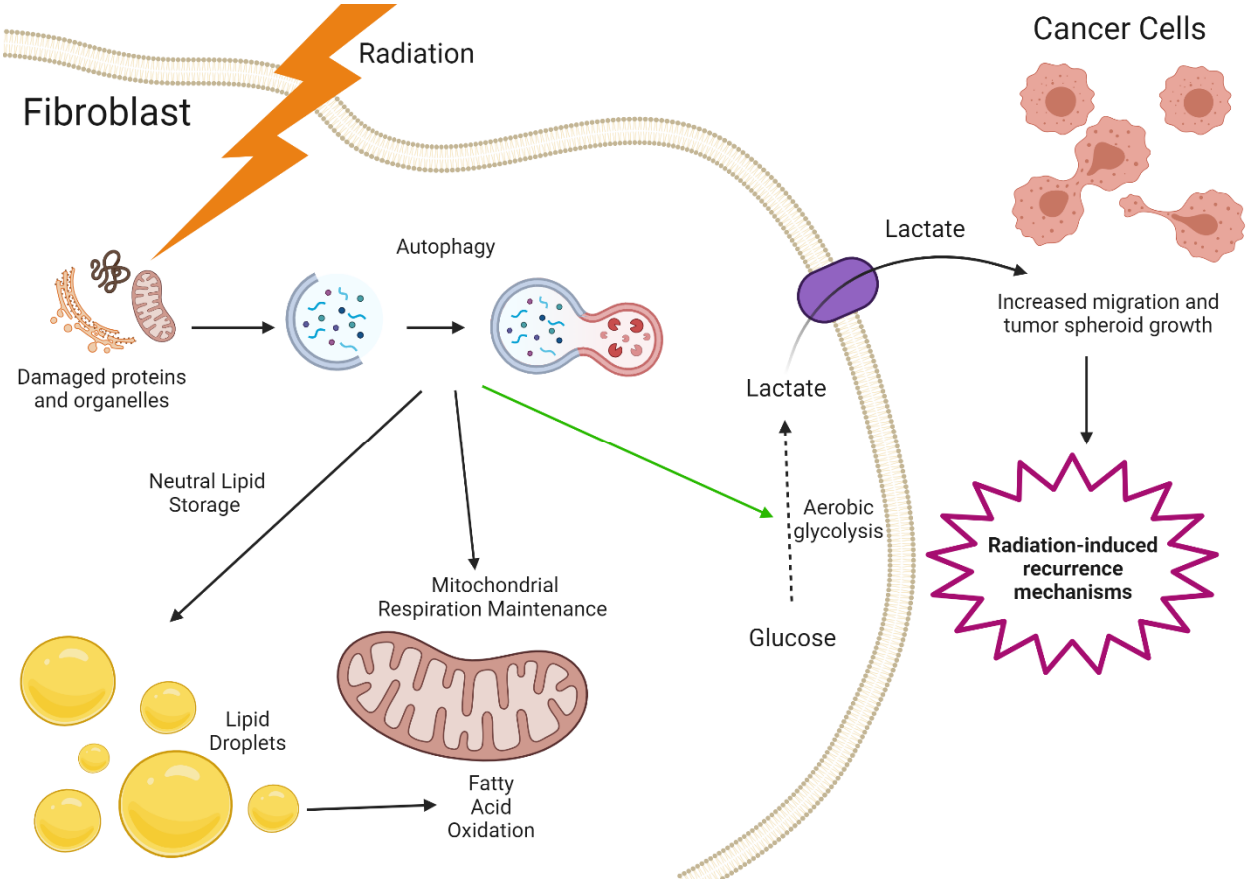

Abbreviations

$4T1^{luc}$: Luciferase-labeled 4T1 mouse mammary carcinoma cells

CAF: Cancer associated fibroblast

CD36: fatty acid translocase

CM: Conditioned media

CQ: Chloroquine

CTC: Circulating tumor cell

DMSO: Dimethyl sulfoxide

ECAR: Extracellular acidification rate

ECM: Extracellular matrix

FAO: Fatty acid oxidation

FASN: Fatty acid synthase

FCCP: Carbonyl cyanide-p-trifluoromethoxyphenylhydrazone

γ-H2AX: phospho-histone H2A.X

HBSS: Hank's buffered saline solution

IF: Immunofluorescence

iMF: Immortalized human reduction mammoplasty fibroblast

LC3B: Microtubule-associated protein 1A/1B-light chain 3 B

MCT: Monocarboxylate transporter

NAT: Normal adjacent tissue

OCR: Oxygen consumption rate

ORO: Oil red O

PBS: Phosphate buffered saline

ROS: Reactive oxygen species

SSO: Sulfosuccinimidyl oleate

RT: Radiation therapy

TNBC: Triple negative breast cancer

TCGA BRCA: The Cancer Genome Atlas Breast Invasive Carcinoma

Introduction

Breast cancer, the most diagnosed cancer worldwide, is one of the deadliest forms of cancer for women (Sung et al., 2021). Roughly 15% of breast cancer patients are diagnosed with triple negative breast cancer (TNBC), a highly aggressive and metastatic subtype (Sioshansi et al., 2012; Siegel et al., 2023). Treatment for TNBC typically consists of neoadjuvant chemotherapy, surgery, and adjuvant radiation therapy (RT) (Wapnir and Khan, 2019; Smith et al., 2018). The primary goal of RT is to eliminate residual cancer cells following surgery, and it is largely effective at reducing the incidence of recurrent disease (Darby et al., 2011). Although improved therapies have led to better outcomes and decreased off-target effects, patients with TNBC still experience high locoregional recurrence rates (David Voduc et al., 2010; Lowery et al., 2012; Zhang et al., 2015; Jwa et al., 2016; Adra et al., 2019).

Residual radioresistant cancer cells adopt an altered lipid metabolic profile that may promote recurrence (Havas et al., 2017; Corn et al., 2020). Both increased *de novo* fatty acid synthesis and fatty acid oxidation (FAO) are linked to radioresistance in breast and other cancers treated by RT (Han et al., 2019; Du et al., 2019; Tan et al., 2018; Chuang et al., 2019; Göttgens et al., 2019). Additionally, upregulated FAO has been shown to drive cancer cell resistance to anoikis (Dheeraj et al., 2018; Sawyer et al., 2020; Wang et al., 2018), suggesting that circulating tumor cell (CTC) survival after RT is supported by altered metabolic profiles. The recruitment of breast CTCs to radiation-damaged sites has been identified as a contributing factor to locoregional recurrence beyond residual tumor cells in the irradiated surgical bed (Rafat et al., 2018; Vilalta et al., 2014; Hacker et al., 2023). However, how the stromal cell metabolic response to RT influences recurrence remains unclear.

Fibroblasts are major cellular contributors to the wound healing response to radiation. They are recruited to radiation-damaged sites and secrete new extracellular matrix (ECM) to promote healing, where excess deposition can lead to fibrosis (Rodemann and Bamberg, 1995; Zhao et al., 2019). Fibroblasts within mammary tissue are exposed to off-target effects of RT and may interact with recruited or residual CTCs. Determining how normal tissue fibroblasts metabolically respond to radiation damage is therefore crucial for understanding recurrence. Studies typically focus on cancer-associated fibroblasts (CAFs) and their interactions with tumor cells. CAFs can transfer lipids and fatty acids to (Santi et al., 2015; Auciello et al., 2019) and upregulate lipid synthesis and saturation pathways in tumor cells (Liu et al., 2018; Neuwirt et al., 2020). Upregulated glycolysis in CAFs also plays a critical role in tumor progression through the secretion of lactate, providing an alternate fuel source for oxidative cancer cells (Martinez-Outschoorn et al., 2014; Becker et al., 2020). These studies suggest that irradiated fibroblast

metabolic changes may lead to crosstalk with tumor cells to impact recurrence mechanisms.

Here, we show how radiation damage alters fibroblast metabolism through the analysis of lipid droplet dynamics, autophagic flux, mitochondrial respiration, and aerobic glycolysis. We determine that irradiated fibroblasts are highly energetic and secrete high levels of lactate into the extracellular environment, which directly increases TNBC cell migration rates and tumor spheroid outgrowth. Our study reveals a metabolic recurrence mechanism that can be targeted to improve TNBC patient survival following RT.

Results and Discussion

Irradiated fibroblasts increase TNBC cell growth and accumulate lipid droplets

Since previous work showed that RT-damaged mammary stroma secretes factors that recruit CTCs and promotes TNBC recurrence (Rafat et al., 2018), we first evaluated the effect of secreted factors from irradiated NIH 3T3 murine fibroblasts on 4T1 TNBC cell invasion and growth. Conditioned media (CM) was collected from fibroblasts irradiated to 10 Gy after incubation for 2 or 7 days and used in a transwell invasion assay. CM from irradiated fibroblasts moderately increased 4T1 invasion compared to CM from unirradiated fibroblasts (**Fig. S1A**). Importantly, irradiated fibroblasts promoted a significant increase in 4T1 growth when co-cultured (**Fig. 1A**). These results indicate that interactions between RT-damaged fibroblasts and TNBC cells may impact recurrence. A clonogenic assay demonstrated that fibroblasts are more radioresistant than tumor cells as expected (Vilalta et al., 2014) (**Fig. S1B**), while 3T3s and 4T1s showed similar levels of phospho-histone H2A.X (γ-H2AX) expression following RT up to a dose of 10 Gy (**Fig. S1C–D**). These results suggest that although fibroblasts may experience equivalent levels of DNA damage for the same radiation dose as cancer cells, they are more likely to survive following RT.

Due to the importance of lipid metabolism in radioresistant cancer cells and CTCs, we hypothesized that lipid droplets in fibroblasts may be a critical marker for analyzing post-RT metabolic profiles. We evaluated the expression of perilipin-2 (Sztalryd and Brasaemle, 2017) in the normal adjacent tissue (NAT) of breast cancer patients from The Cancer Genome Atlas Breast Invasive Carcinoma (TCGA BRCA) dataset (Goldman et al., 2020; Koboldt et al., 2012). We observed that patients with high levels of NAT perilipin-2 expression had worse overall survival compared to those with low expression (**Fig. 1B**), indicating an inverse relationship between lipid droplets in the NAT and breast cancer patient survival. We then observed a 2-fold increase in lipid droplets from perilipin-2 staining in irradiated fibroblasts up to 7 days following RT (**Fig. 1C–D**), demonstrating that an altered lipid metabolic profile persists well after the initial

cellular stresses of RT. We also measured decreased perilipin-2 expression in the lipid droplets of irradiated fibroblasts starting at 3 days after RT, suggesting these neutral lipid stores may be more susceptible to lipolysis, degradation, and utilization by the cells (Xu et al., 2019) (**Fig. S1E**). To confirm perilipin-2 expression correlated with increased neutral lipid storage after RT, we stained fibroblasts for Oil Red O (ORO; **Fig. 1E–F**). More than a 2-fold increase in lipid droplet area in irradiated fibroblasts was observed (**Fig. 1F**), and this neutral lipid increase was also shown with BODIPY 493/593 flow cytometry analysis (**Fig. S1F–G**). We additionally confirmed these trends in immortalized human reduction mammoplasty fibroblasts (iMFs; **Fig. 1G–H, Fig. S1H**).

Irradiated fibroblasts increase extracellular fatty acid uptake, but inhibition does not impact lipid storage

Increased lipid storage following radiation damage has been demonstrated in macrophages (Katayama et al., 2008) and dendritic cells (Gao et al., 2015). Although this phenomenon has been observed when these cells are recruited to areas of radiation damage, these studies suggest extracellular metabolites may be the source of increased lipid droplets, with either anabolism or the direct uptake of fatty acids. We therefore evaluated the expression of fatty acid synthase (FASN) and saw no significant differences between irradiated and unirradiated fibroblasts (**Fig. S2A–B**). We then incubated both irradiated and control fibroblasts with BODIPY-conjugated palmitate, which showed increased fatty acid uptake in irradiated cells (**Fig. 2A–B**), especially starting at 3 days after RT. These results correlated with our findings showing increased neutral lipid storage in irradiated fibroblasts. To evaluate the impact of increased fatty acid uptake on lipid droplets, sulfosuccinimidyl oleate (SSO) was used to inhibit the fatty acid translocase enzyme (CD36). While CD36 inhibition reduced fatty acid uptake by approximately 50% (**Fig. S2C**), this surprisingly resulted in either no change or a slight increase in post-RT neutral lipid storage as observed through ORO staining (**Fig. S2D**). These results suggest that irradiated fibroblasts rely in some capacity on extracellular fatty acids for lipid metabolism following RT, but an alternate pathway is responsible for lipid accumulation in irradiated fibroblasts.

Radiation-induced autophagy promotes neutral lipid accumulation

Autophagy has been demonstrated in tumor cells as a mechanism for the removal of biomolecules and cellular compartments damaged by reactive oxygen species (ROS) generated from RT (Huang et al., 2014; Wang et al., 2015). We hypothesized that activation of autophagy

in irradiated fibroblasts and the degradation of lipid membranes in damaged organelles results in increased lipid storage similar to lipid accumulation following starvation-induced autophagy (Nguyen et al., 2017). We analyzed the presence of acidic lysosomes in RT-treated fibroblasts through LysoTracker staining (**Fig. 2C**). We observed a significant increase in lysosome formation and acidification starting at day 3 following RT in irradiated fibroblasts, which persisted 7 days after RT (**Fig. 2D**). We evaluated the formation of autophagosomes through immunofluorescence (IF) staining of microtubule-associated protein 1A/1B-light chain 3B (LC3B) (Mizushima et al., 2010). Irradiated cells exhibited bright LC3B puncta formation starting 3 days after RT (**Fig. 2E–F**), suggesting that autophagy is upregulated during the period of RT-induced lipid accumulation.

Although increased lysosomal staining and LC3B puncta formation may indicate increased autophagic flux, these results can also be observed in cells with defective autophagy (Runwal et al., 2019), which has been demonstrated in radiation-damaged cells (Endo et al., 2020). To confirm if there was increased autophagic flux in irradiated fibroblasts, we inhibited autophagy using chloroquine (CQ). CQ treatment successfully resulted in a decrease in lysosomal acidification 3 days after RT (**Fig. S2E**). Staining for LC3B in CQ-treated irradiated cells showed a substantial increase in LC3B positive structures, confirming an increase in autophagic flux (**Fig. 2G–H**). Additionally, CQ treatment of unirradiated cells increased LC3B expression, indicating that normal fibroblasts have a low basal level of autophagy. Inhibition of autophagy led to a substantial decrease in lipid droplet formation in irradiated fibroblasts as evaluated through ORO (**Fig. 2I**) and perilipin-2 IF analysis (**Fig. S2F**). We confirmed that autophagy also drives post-RT lipid accumulation in human fibroblasts (**Fig. 2J**).

Metabolic flux analysis reveals increased mitochondrial respiration is linked to autophagy and FAO in irradiated fibroblasts

We next stained fibroblasts with MitoTracker Deep Red to evaluate a baseline level of mitochondrial dynamics following RT using flow cytometry analysis. Increased staining indicates either increased mitochondrial mass or membrane potential (Mauro-Lizcano et al., 2015; Xiao et al., 2016). We observed that irradiated cells had higher MitoTracker intensity compared to unirradiated cells (**Fig. 3A**). Interestingly, autophagy inhibition increased MitoTracker intensity for both irradiated and unirradiated cells (**Fig. 3B**). These results suggest that increased MitoTracker staining in irradiated cells following autophagy inhibition is due to damaged or dysfunctional mitochondria that are not degraded by autophagolysosomes. To determine the mechanism behind increased MitoTracker staining, we evaluated mitochondrial bioenergetics

through a modified mitochondrial stress test, which allowed us to perform a metabolic flux analysis with autophagy inhibition (**Fig. S3A–B**). Irradiated fibroblasts had a roughly 3-fold increase in ATP-linked oxygen consumption rate (OCR) compared to unirradiated fibroblasts (**Fig. 3C**), matching observations of increased MitoTracker staining. Autophagy inhibition completely abrogated the large ATP-linked OCR increase in irradiated fibroblasts. These results indicate that autophagy-inhibited MitoTracker staining in irradiated fibroblasts is related to an increase in defective mitochondrial biomass, which reveals that autophagy is critical for recycling damaged mitochondria to maintain higher mitochondrial respiration after RT. In addition, non-mitochondrial OCR was observed to be substantially higher in irradiated fibroblasts compared to unirradiated controls (**Fig. 3D**). This suggests that organelles and proteins are being damaged well after the initial events of RT since non-mitochondrial OCR has been linked to increased activity of intracellular oxidases that generate ROS (Dranka et al., 2010; Hill et al., 2012; Chacko et al., 2014).

We then examined whether the higher basal and mitochondrial-linked OCRs in irradiated fibroblasts were the result of increased FAO from the post-radiation increase in neutral lipid stores. We performed the mitochondrial stress test with the addition of etomoxir to inhibit FAO. Extracellular fatty acids were absent during the test to limit the source of lipids for FAO to be intracellular. We observed a roughly 40% reduction in ATP-linked OCR rates following incubation of etomoxir (**Fig. 3E, S3A–B**). These results suggest that lipid stores are being used for FAO in irradiated cells and are responsible for a significant portion, but not the entirety, of post-RT increases in ATP-linked OCR.

We analyzed the corresponding extracellular acidification rate (ECAR) in irradiated cells during the modified mitochondrial stress test. At 3 days after RT, irradiated and unirradiated fibroblasts showed equivalent basal ECAR, and this ECAR was not impacted by autophagy inhibition. However, after 7 days, irradiated fibroblasts exhibited an increase in basal ECAR which was abrogated upon autophagy inhibition (**Fig. 3F**). These results show that autophagy is essential in maintaining increased aerobic glycolysis in irradiated fibroblasts at late timepoints following radiation damage. We then performed a modified glycolytic stress test at 7 days after RT, where ECAR in irradiated and unirradiated fibroblasts was measured in response to a bolus of glucose in saturating levels of glutamine without sodium pyruvate (**Fig. S3C–D**). Irradiated fibroblasts indeed demonstrated increased glycolytic ECAR, suggesting increased aerobic glycolysis (**Fig. 3G**). Only the reserve glycolytic ECAR in irradiated cells showed major differences upon autophagy inhibition (**Fig. 3H**), indicating that autophagy is important in maintaining the ability of irradiated fibroblasts to switch from mitochondrial respiration to

glycolysis. An increase in aerobic glycolysis in irradiated fibroblasts 7 days after RT was further supported by an increase in intracellular pyruvate levels from lysates of irradiated fibroblasts compared to unirradiated controls (**Fig. S3E**). Notably, we determined a substantial decrease in Ki67-positive cells within the irradiated fibroblast population, suggesting that increased aerobic glycolysis was not the result of the selection of a radioresistant population (**Fig. S3F**). We also performed the modified glycolytic stress test 7 days after RT with and without autophagy inhibition in human iMFs (**Fig. S3G–H**). A substantial increase in glycolytic ECAR was observed in the irradiated iMFs compared to unirradiated controls, and autophagy directly maintained the high ECAR levels (**Fig. 3I**). Additionally, irradiated iMFs at 7 days after RT exhibited more than a 2-fold increase in ATP-linked OCR compared to unirradiated cells (**Fig. 3J**). Autophagy inhibition did not directly reduce this ATP-linked OCR in the human iMFs, suggesting that autophagy may be more important for maintaining aerobic glycolysis than mitochondrial respiration in human cells. Taken together, these results indicate that evaluating metabolic crosstalk between irradiated fibroblasts and TNBC cells by way of aerobic glycolysis may elucidate recurrence mechanisms.

Increased radiation-induced aerobic glycolysis in fibroblasts promotes lactate secretion and metabolic crosstalk with TNBC cells

We hypothesized that secreted factors from irradiated fibroblasts directly influence TNBC cells. We incubated TNBC cells with CM collected from irradiated 3T3s 7 days after RT and observed decreased LysoTracker live cell staining intensity (**Fig. 4A, S3I**) and decreased autophagosome formation by 75% (**Fig. 4B, S3J**). These results suggest a metabolite specifically from irradiated fibroblasts decreases basal levels of autophagy in TNBC cells. Based on the observed increased aerobic glycolysis, we determined that irradiated fibroblast CM contained an approximately 5 mM increase in L-lactate concentration compared to unirradiated fibroblast CM (**Fig. 4C**). We used the small molecule inhibitor AZD3965 to block lactate uptake through monocarboxylate transporters MCT1/2 in TNBC cells (Draoui and Feron, 2011), which has been utilized in phase 1 breast cancer clinical trials (Benyahia et al., 2021). We used 50 nM AZD3965 to optimize TNBC proliferation effects as a result of the inhibition of lactate uptake (**Fig. S3K**).

We next conducted a scratch-wound assay (**Fig. 4D**) where TNBC cells were exposed to either irradiated or unirradiated fibroblast CM, and the closure of the gap was observed over 15 hours. TNBC cells incubated in irradiated fibroblast CM closed the gap at a significantly higher rate, and this increase was eliminated with the addition of AZD3965 (**Fig. 4E**). These results suggest that increased lactate secretion from irradiated fibroblasts enhances migration rates of

TNBC cells. Since CTCs have been shown to survive detached from the ECM due to increased mitochondrial respiration, and lactate can supply citric acid cycle intermediates, we evaluated how irradiated fibroblast secreted factors influence tumor spheroid growth. Spheroids grown in irradiated fibroblast CM experienced higher outgrowth compared to those grown in unirradiated fibroblast CM (**Fig. 4F–G**), and the addition of AZD3965 completely abrogated this outgrowth. The combined impact of increased migration and increased spheroid outgrowth in TNBC cells incubated with CM from irradiated cells suggests that fibroblasts induce an aggressive phenotype in TNBC cells following RT.

We established a link between post-RT lipid accumulation, autophagy, and aerobic glycolysis, which impacted metabolic crosstalk between irradiated fibroblasts and TNBC cells. To determine the connection between these mechanisms in human tissue, we evaluated gene expression data for *Map1lc3b* (LC3B), *Lipa* (lipase A), and *Ldha* (lactate dehydrogenase) in patient NAT. We found strong correlations with the expression of each of these genes against expression of *Plin2* (**Fig. 4H**), which was also associated with overall worse survival for breast cancer patients (**Fig. 1C**). These analyses further implicate lipid metabolism, autophagy, and lactate generation in TNBC recurrence post-therapy.

Concluding Remarks

In this study, we demonstrate how radiation impacts fibroblast metabolism and, ultimately, metabolic crosstalk between fibroblasts and TNBC cells. We used lipid droplets as a marker for metabolic alterations in radiation-damaged fibroblasts since a reliance on FAO has been shown to be critical in tumor progression, radioresistance, and CTC survival (Han et al., 2019; Sawyer et al., 2020). We observed increased neutral lipid storage in irradiated fibroblasts compared to unirradiated cells and found autophagy to be critical in maintaining these stores. Additionally, irradiated fibroblasts had a significant increase in extracellular fatty acid uptake and FAO, demonstrating the importance of lipid metabolism to the post-RT survival of fibroblasts. Exactly how irradiated fibroblasts utilize extracellular fatty acids and why this flux is increased after radiation remains to be determined. We further showed that irradiated fibroblasts displayed increased ATP-linked respiration, aerobic glycolysis, and reserve glycolytic capacity, which was maintained through increased autophagic flux, indicating irradiated fibroblasts are highly metabolically active for a significant amount of time following RT. This increased metabolic activity may be critical for post-RT survival and could serve as a communication channel to immune cells through the generation of cytokines and other metabolic intermediates that act as damage signals (Mu et al., 2018; Manoharan et al., 2021). The production of these molecules is

common in senescent cells (Sabbatinelli et al., 2019), and the observed decrease in Ki67-positive cells after RT may indicate senescence (Zorin et al., 2017). Due to the observed increased lactate efflux from irradiated fibroblasts and studies demonstrating that lactate secreted from CAFs is important for tumor progression (Martinez-Outschoorn et al., 2014; Becker et al., 2020), we showed that blocking TNBC cell uptake of RT-induced fibroblast lactate decreased migration and spheroid outgrowth.

While we focused on metabolic crosstalk between irradiated fibroblasts and TNBC cells, stromal-immune cell interactions are also important in the irradiated microenvironment. Neutrophils and macrophages are recruited to sites of radiation damage, and both of these innate immune cells have been implicated in post-RT TNBC recurrence mechanisms (Sherry et al., 2020; Rafat et al., 2018; Hacker et al., 2023). In the tumor microenvironment, acidosis and increased lactate secretion by tumor cells have been shown to promote anti-inflammatory and pro-tumorigenic polarization of these immune cells, and lactate secretion from irradiated fibroblasts may promote similar polarization patterns (Wang et al., 2021; Deng et al., 2021; Mu et al., 2018; Noe et al., 2021). Adipocytes, another abundant cell type in the breast tissue microenvironment, have been demonstrated to influence the fibroblast radiation damage response (Kosmacek and Oberley-Deegan, 2020). Adipocyte lipid metabolic response to radiation may alter extracellular fatty acid availability for fibroblasts, impacting autophagy and lipid metabolism in fibroblasts damaged by radiation. These insights highlight the need to evaluate changes in cellular metabolism following RT in multiple cell types under microenvironmental stressors to determine novel therapies to prevent recurrence. Our study provides a link between metabolic profiles in fibroblasts post-radiation and metabolic crosstalk with cancer cells that leads to an aggressive TNBC phenotype.

Materials and Methods

Cell culture. NIH 3T3 murine embryonic fibroblasts were obtained from ATCC and immortalized human reduction mammoplasty fibroblasts (iMFs) were obtained from Dr. Charlotte Kuperwasser (Tufts University) in April 2022. Fibroblasts were cultured in high glucose DMEM (Gibco 11995-065) containing 10% bovine calf serum and 1% penicillin/streptomycin. Luciferase-labeled 4T1 mouse mammary carcinoma cells ($4T1^{luc}$) were obtained from Dr. Christopher Contag (Stanford University) in August 2011, and unlabeled 4T1 cells were obtained from ATCC. 4T1 TNBC cells were cultured in RPMI 1640 medium (Gibco 11875-093) containing 10% heat-inactivated fetal bovine serum and 1% penicillin/streptomycin. All cells were maintained at 37°C in a humified incubator containing 5% CO_2 and were routinely evaluated for the presence of mycoplasma using the Myco-Sniff-Rapid™ Mycoplasma Luciferase Detection Kit (MP Biomedicals 0930504-CF).

Radiation. For radiation experiments, cells were grown to 70% confluency in T300, T75, or T25 flasks and then irradiated to a dose of 10 Gy using a cesium source. Following irradiation, cells were immediately plated into new plates or flasks with fresh media. Cell counts at the indicated post-RT timepoints were kept constant between irradiated and non-irradiated cells.

Clonogenic assays and DNA damage analysis. 3T3s were irradiated to doses up to 10 Gy and plated in 6 or 10 cm dishes in normal growth media in triplicate at appropriate concentrations. After 12 days, colonies were stained with 0.25% w/v crystal violet solution in 95% ethanol and counted, and the surviving fraction was calculated by dividing the number of colonies by the initial number of cells plated and normalized to the 0 Gy surviving fraction. The survival data was fitted with the linear-quadratic model ($\text{Surviving Fraction} = e^{-(\alpha * Dose + \beta * Dose^2)}$). For DNA damage analysis, cells on glass coverslips were irradiated to doses up to 10 Gy. Cells were fixed for IF staining of γ-H2AX 30 minutes following RT (Kuo and Yang, 2008; Kinner et al., 2008).

Fibroblast CM and lactate concentration. Irradiated and unirradiated 3T3s were plated in T25 flasks in complete growth media for either 2 or 7 days, at which point supernatant was collected and filtered through a 0.2 µm filter to remove cell debris. Cell counts between irradiated and unirradiated flasks at the time of CM collection were kept constant. Filtered CM was stored at –80°C until use. L-lactate concentration in CM was determined using Cayman Chemical's L-Lactate Assay Kit (700510) following the manufacturer's instructions. When 4T1s were

incubated in fibroblast CM, complete media was removed 24 hours prior to 70% confluency, washed with phosphate buffered saline (PBS), and replaced with CM for incubation at 37°C.

Invasion assays. CM from irradiated and control 3T3s at the 2- and 7-day post-RT timepoints was used as the chemoattractant in a transwell invasion assay. $1x10^5$ luciferase-labeled $4T1^{luc}$ cells were placed in upper chambers of migration (Corning, BioCoat PET control inserts, 8 µm pore size) or invasion inserts (Corning, BioCoat growth-factor reduced Matrigel invasion matrix, 8 µm pore size) in duplicate and were allowed to migrate toward the chemoattractant for 24 hours. Cells that migrated or invaded through membranes were fixed in methanol, mounted on slides with ProLong glass antifade mountant with NucBlue stain (Invitrogen P36981), and counted. The invasive index was calculated by dividing the number of cells on invasion inserts by the number of cells on migration inserts. Migration and viability were confirmed by imaging the $4T1^{luc}$ cells that migrated through the membranes to the 24 well receiver plate using bioluminescence imaging. For bioluminescence readings, an IVIS Lumina Series III (Caliper LifeSciences) was used. Cells were imaged after incubation with 0.167 mg/mL Luciferin (Biosynth L-8220) for 10 minutes.

Co-culture. $4T1^{luc}$ cells were co-cultured with irradiated or unirradiated 3T3s at 6 days following RT for 48 hours in 6 well tissue culture treated plates, with experiments ending at 8 days following RT. Seeding densities of fibroblasts were adjusted so that the same number of irradiated or unirradiated fibroblasts were present at the end of the 48 hour co-culture period. Bioluminescence imaging was performed to determine cell density, and the total flux of the co-culture was normalized to total flux of $4T1^{luc}$ cells in basal fibroblast media.

TCGA patient data analysis. The TCGA BRCA dataset (Koboldt et al., 2012) was accessed through the University of California Santa Cruz Xena platform on March 31st, 2022 to evaluate how gene expression of *Plin2* in the normal adjacent tissue (NAT) of breast cancer patients correlated with overall survival, and to analyze co-expression with *Map1lc3b, Lipa, and Ldha* (Goldman et al., 2020). The Xena visualization tool was utilized (https://xenabrowser.net/) to first access the TCGA BRCA dataset, and then only Solid Tissue Normal sample types were kept for analysis. Subsequently, “Breast” was selected as the primary site to only include patient data from TCGA from breast cancer patients. These selections yielded a total patient dataset of n = 113 NAT samples. *Plin2* was then entered to evaluate gene expression data via RNAseq analysis, and a Kaplan Meier curve was generated utilizing the built-in functionality of the Xena

platform. *Map1lc3b, Lipa, and Ldha* were subsequently entered to collect gene expression data and evaluate linear correlation with *Plin2*, where Pearson correlation coefficients were calculated.

Neutral lipid staining. Oil Red O (Sigma O0625) and BODIPY 493/503 (Invitrogen D3922) dyes were used for neutral lipid detection in cells. For ORO staining, 0.5 g of ORO powder was added to 100 mL of propylene glycol, heated at 97°C for 30 minutes, and stored at room temperature until use. Prior to staining, the ORO solution was vacuum filtered through a 0.45 µm filter. Cells on glass coverslips were fixed in neutral-buffered formalin for 20 minutes at room temperature, washed three times in PBS, and then incubated in propylene glycol for 2 minutes. Following removal of the propylene glycol, coverslips were incubated in ORO solution for 2 hours at room temperature. Samples were then differentiated in 85% propylene glycol for 5 minutes, rinsed in PBS, stained with hematoxylin for 45 seconds, rinsed in DI water, and mounted onto glass slides using a glycerin solution. For BODIPY 493/503 staining, cells were labeled with a 2 µM solution for 30 minutes at 37°C (Qiu and Simon, 2016).

Immunofluorescence staining. For perilipin-2, fatty acid synthase, γ-H2AX, and Ki67 staining, which required permeabilization, cells on glass coverslips fixed in neutral-buffered formalin were incubated in a 0.1% Triton X-100 solution (Sigma X100) for 10 minutes. For LC3B staining, cells were fixed and permeabilized in 100% ice-cold methanol for 10 minutes at -20°C. Cells were blocked for 1 hour at room temperature with 10% normal goat serum (Vector Labs S-1000) and then incubated overnight at 4°C in a humidified chamber with anti-γ-H2AX (1:500, Invitrogen MA5-38225), anti-perilipin-2 (1:200, Invitrogen MA5-32664), anti-fatty acid synthase (1:50, Invitrogen MA5-14887), anti-LC3B (1:200, Abcam ab192890), and anti-Ki67 (1:200, Invitrogen MA5-14520) in 1% bovine serum albumin (Sigma A1470) and 0.1% Tween-20 (Sigma P1379). Coverslips were mounted onto slides using ProLong Glass Antifade Mountant with NucBlue following secondary antibody incubation with goat anti-rabbit IgG AlexaFluor 488 (1:200, Invitrogen A-11008) or goat anti-rabbit IgG AlexaFluor 594 (1:200, Invitrogen A-11012). A corresponding no primary antibody control was performed for all conditions to confirm specificity.

Microscopy, image processing, and quantification. Stained samples were imaged using a Leica DMi8 inverted microscope with Leica DFC9000GT sCMOS fluorescence and Leica MC190 HD digital cameras. For fluorescence microscopy, a Lumencor mercury-free SOLA light

engine was used for the illumination source. For live cell imaging, cells were imaged using an Okolab Bold Line CO_2 and temperature unit with air pump. The microscope was fitted with DAPI, GFP, TXR, and Y5 filter cubes. Images (8 bit) were captured using LASX imaging software. Images of perilipin-2 and LC3B staining were captured as Z-stacks. All images were analyzed using Fiji software (Schindelin et al., 2012). For ORO neutral lipid quantification, deconvolution of RGB images to evaluate the ORO-stained area was performed using the built-in H&E vector, and positive area was normalized by number of cells. For all IF imaging, area of positive staining was set based on the no primary control images and thresholded accordingly. Z-stacks were merged using maximum intensity projections. For γ-H2AX, expression was calculated by multiplying staining intensity by area of positive staining and normalizing to nuclear area. For Ki67, the number of cells with positive staining were divided by the total number of cells within the image to calculate the percentage of positive cells. For all other IF analysis, expression multiplied by staining area or area of positive staining was normalized by cell number.

BODIPY-labeled palmitate uptake experiments and CD36 inhibition. BODIPY FL C_{16} (4,4-Difluoro-5,7-Dimethyl-4-Bora-3a,4a-Diaza-*s*-Indacene-3-Hexadecanoic Acid, Invitrogen D3821) was used to assess the ability of 3T3s to transport fatty acids into the cell from their surroundings. Uptake experiments were performed using modified pre-established protocols (Somwar et al., 2011). Briefly, fibroblasts were washed in serum free media and incubated in DMEM containing 0.5% fatty acid free bovine serum albumin (Fisher BP9704100) containing 10 µM BODIPY FL C_{16} for 40 minutes at 37°C. Cells were then washed with 0.5% albumin-containing media and incubated with 1.5 µM of Hoechst 33345 (ThermoScientific) for 20 minutes. Cells were washed and imaged live at 37°C and 5% CO_2 in Hank's buffered saline solution (HBSS, Corning 21-023-CV). The relative amount of BODIPY FL C_{16} taken up by irradiated and unirradiated control cells was determined by multiplying the area of positive staining by the intensity and normalizing by cell count using Fiji. To inhibit fatty acid uptake, sulfosuccinimidyl oleate (SSO, MedChemExpress HY-112847A), an irreversible inhibitor of fatty acid translocase (CD36) was used. Increasing concentrations of SSO (10 – 500 µM) dissolved in dimethylsulfoxide (DMSO) were used in conjunction with BODIPY FL C_{16} to determine maximal inhibition of palmitate uptake in unirradiated cells. A concentration of 50 µM was used in conjunction with a DMSO control for all other extracellular fatty acid uptake inhibition tests.

Autophagy analysis and inhibition. Autophagy was evaluated based on lysosomal

acidification and the presence of LC3B-positive structures in 3T3 fibroblast and 4T1 TNBC cells. LysoTracker Red DND-99 (Invitrogen L7528) was used to identify lysosomal structures. Irradiated or unirradiated 3T3s or 4T1s incubated in fibroblast CM were seeded in tissue culture treated 24 well plates at appropriate seeding densities based on the timepoint after RT and incubated with 50 nM of LysoTracker Red DND-99 and 1.5 μM of Hoechst 33345 solution in media for 30 minutes at 37°C. Following incubation, cells were washed with and imaged live in HBSS at 37°C and 5% CO_2. Lysosomal acidification was quantified by calculating the product of the area of positive staining and the staining intensity using Fiji and normalizing by the number of cells per field of view. For autophagosome analysis, irradiated or unirradiated 3T3 fibroblast or 4T1 TNBC cells incubated in fibroblast CM were seeded on glass coverslips at appropriate seeding densities. 3T3 or 4T1 cells were stained for LC3B as described previously. Autophagosomes were identified by the formation of bright puncta compared to diffuse LC3B IF staining in the cytoplasm (Mizushima et al., 2010). These puncta were analyzed by thresholding after subtracting background fluorescence using Fiji, and the cross-sectional area per cell was calculated to represent the number of autophagosomes in the cell. This area was then normalized by dividing by the average of all conditions within each biological replicate. Chloroquine diphosphate salt (CQ, Sigma C6628) was used as an autophagy inhibitor. 5 hours prior to the indicated timepoint, 3T3 cells were incubated with 100 μM of CQ, and iMFs were incubated with 250 μM of CQ in complete media. Control cells were treated with equivalent volumes of PBS. After 5 hours of inhibition (Klionsky et al., 2016), cells were washed and either fixed for ORO or IF staining, imaged live for LysoTracker experiments, or prepared for metabolic flux analysis. Autophagic flux was confirmed by an increase in autophagosomes following CQ inhibition.

Mitochondrial staining. MitoTracker Deep Red (Invitrogen M22426) was used to evaluate mitochondria in 3T3 cells. Stock powder was dissolved in DMSO and used at a working concentration of 200 nM. Cells were washed with PBS and stained with MitoTracker Deep Red in serum free media for 30 minutes at 37°C. Following incubation, cells were washed twice with complete media and then prepared for flow cytometry analysis.

Flow cytometry. Fibroblasts were analyzed via flow cytometry to evaluate BODIPY staining for lipid droplets and MitoTracker Deep Red staining for mitochondrial membrane potential following RT with or without autophagy inhibition (100 μM CQ for 5 hours). At the appropriate timepoints following RT and/or inhibition, cells were stained for MitoTracker Deep Red and

BODIPY for 30 minutes at 37°C. Cells were trypsinized, pelleted, and resuspended in ice cold PBS at a concentration of $1x10^6$ cells/mL. Live cells were determined using a live/dead aqua viability kit (Life Technologies L34966) following the manufacturer's instructions, and staining occurred for 30 minutes on ice. Cells were spun down and resuspended in neutral buffered formalin for 10 minutes on ice for fixation. Cells were then resuspended in 100 µL PBS and analyzed on the Amnis CellStream flow cytometer (Cytek Biosciences). A compensation matrix was generated using single-stained cells and an all-dead sample generated from incubation in 70% ice cold methanol in PBS for 10 minutes. Cells were gated on live and single cells. The compensation matrix and data analysis were performed using FlowJo software. Fluorescence intensity was plotted normalized to the mode for each sample.

Metabolic flux analysis with autophagy and FAO inhibition. Fibroblast mitochondrial oxidative phosphorylation was evaluated through the real-time measurement of the oxygen consumption rate (OCR) and glycolysis through the measurement of the extracellular acidification rate (ECAR) using the Seahorse XFe96 Extracellular Flux Analyzer (Agilent) at the Vanderbilt High Through Screening Core. 3T3 or iMF cells irradiated to a dose of 10 Gy (1,500 3T3 cells/well or 1,400 iMF cells/well) or unirradiated cells (2,200 3T3 cells/well or 1,800 iMF cells/well) were seeded in an XFe96 culture microplate (Agilent 101085-004) and incubated overnight in complete growth media. The sensor cartridge from the Extracellular Flux Assay Kit (Agilent) was hydrated in sterile DI water overnight at 37°C in a non-CO_2 incubator. Five hours prior to the experiment, cells were incubated with basal fibroblast media with either 100 µM CQ, 40 µM etomoxir sodium salt hydrate (Sigma E1905) for FAO inhibition, or an equivalent volume of PBS. The sensor cartridge was incubated with Seahorse XF Calibrant (Agilent 100840-000) 1 hour prior to the experiment, and fibroblasts were washed and then incubated for 1 hour in a non-CO_2 incubator in XF DMEM Medium, pH 7.4 (Agilent 103575-100) supplemented with 2.0 mM L-glutamine (Sigma G8540), 1.0 mM sodium pyruvate (Sigma S8636), and 10 mM D-(+)-glucose (Sigma G7528). The Seahorse XF Cell Mito Stress Test (Agilent 103015-100) or the Seahorse XF Glycolysis Stress Test (without sodium pyruvate or glucose, Agilent 103020-100) were then performed, and injection strategies were followed per the manufacturer's instructions. The following final concentrations of injected drugs and metabolites for both the Mito and Glycolysis Stress Tests were determined from initial optimization experiments: 1.5 µM oligomycin to block ATP synthase, 1.0 µM carbonyl cyanide-p-trifluoromethoxyphenylhydrazone (FCCP) to demonstrate maximal respiration, 0.5 µM of a mixture of rotenone and antimycin A to determine non-mitochondrial respiration, 100 mM glucose for the Glycolytic Stress Test, and

500 mM 2-deoxyglucose to block glycolysis. Cells were counted following the experiment to normalize data per 1,000 cells. Data were analyzed using Seahorse Wave Desktop Software (Agilent), where a background well correction was applied. The following calculations were performed on a per well basis: ATP-linked respiration was calculated as the difference between the baseline and post-oligomycin injected OCRs; non-mitochondrial OCR was determined by levels following rotenone and antimycin A injection; glycolytic ECAR was determined as the difference between the baseline and post-glucose injected ECARs; and reserve ECAR was calculated as the difference between post-glucose injected ECAR and ECAR measured following oligomycin injection.

Intracellular pyruvate analysis. 3T3 cells were analyzed for intracellular pyruvate pools. Cell lysates were collected after cells were plated in 10 cm dishes, washed with ice cold PBS, and incubated with RIPA Buffer (Sigma R0278) containing 5 mM EDTA (Corning 46-034-CI), 1 EDTA-free mini cOmplete EASYpack tablet (Roche 04693159001), and 1 mini PhoSTOP EASYpack tablet (Roche 04906845001). Following cell lysis, supernatant was collected, incubated on ice for 30 minutes, and spun down at 4°C at 13,300xg. Supernatant was collected and stored at -80°C until use. Intracellular pyruvate concentrations were determined using the pyruvate analysis component of the EnzyChrom Aspartate Assay Kit (Bioassay Systems EASP100) following the manufacturer's instructions. Concentrations were normalized to total protein determined from a Pierce BCA protein assay kit (Thermo Scientific 23227).

Lactate uptake inhibition. AZD3965 (MedChemExpress HY-12750) was used to inhibit lactate uptake in 4T1 cells. To evaluate the initial impact of AZD3965 on $4T1^{luc}$ cell proliferation and lactate uptake, cells were incubated for 24 hours in basal 4T1 media with varying concentrations of AZD3965 in a 24 well tissue culture treated plate, at which point bioluminescence imaging was performed. Total flux for each AZD3965 concentration was normalized to the total flux for cells incubated with a DMSO control. 50 nM of AZD3965 was utilized in all lactate uptake inhibition experiments and compared to a DMSO control.

Scratch wound assay. 4T1 cells were plated in 2-well culture inserts in µ-dishes (Ibidi 81176) at 2.15×10^5 cells/mL in normal culture media for 36 hours, after which inserts were removed to create a cell-free gap representing the wound scratch. The µ-dishes were washed with PBS and incubated with 7-day post-RT 3T3 CM supplemented with 50 nM AZD3965 or an equivalent volume of DMSO (control). Phase contrast images were taken every 3 hours up to 15 hours.

The scratch wound area was calculated in Fiji as the cell-free space between the leading edge of the cells. Scratch wound closure percentage was calculated by dividing scratch wound area by the area at the start of the assay.

Tumor spheroids. 4T1 cells were plated at $2x10^4$ cells per well in 200 uL of 7-day post-RT 3T3 CM supplemented with either 50 nM AZD3965 or an equivalent volume of DMSO (control) in a Nunclon Sphera ultra-low attachment 96-well U-bottom plate (Thermo Scientific 174929), allowing the cells to form spheroids. Spheroid outgrowth was calculated based on cross-sectional area analyzed from phase contrast images taken at 3, 6, and 9 days after plating.

Statistical analysis. Fibroblast radiation dose dependence was evaluated using a linear-quadratic model. The log-rank test was used to determine statistical significance in Kaplan-Meier analysis. An unpaired, 2-sample t-test was used within timepoints to evaluate BLI measurements from 4T1s co-cultured with 3T3s, perilipin-2 and ORO lipid droplet analyses without inhibition, BODIPY-C16 uptake, lysosomal acidification without inhibition in both 3T3s and 4T1s, autophagosome cross-sectional area in 3T3s without inhibition, 4T1 scratch-wound closure times, concentration of L-lactate in fibroblast CM, intracellular pyruvate levels, and Ki67 expression. Autophagosomal area, lysosomal acidification, and lipid droplet analyses from ORO and perilipin-2 staining with inhibition were analyzed in a general linear model (ANOVA), along with OCR and ECAR analyses from Seahorse. A Mann-Whitney test for non-normally distributed distributions was used to analyze tumor spheroid outgrowth and 4T1 autophagosome cross-sectional area. Post hoc analyses were performed with either a Tukey or Games-Howell adjustment for multiple comparisons for equal and non-equal variances, respectively. Pearson correlation coefficients were calculated to evaluate correlation between genes from the TCGA BRCA dataset. All analyses were performed using Minitab 18.

Supplemental Material

Fig. S1 shows relative radiosensitivities of 3T3 fibroblast and 4T1 TNBC cells as well as additional characterization of post-RT lipid droplet dynamics in fibroblasts through perilipin-2 intensity analysis and BODIPY flow cytometry analysis. **Fig. S2** shows FASN expression analysis in fibroblasts following RT, evaluation of inhibition of lipid uptake on fibroblast lipid droplets, and additional analysis of the impact of autophagy inhibition on fibroblast lipid droplets through perilipin-2 analysis. The figure also demonstrates the abrogation of lysosomal acidification in irradiated fibroblasts upon chloroquine incubation. **Fig. S3** shows representative

OCR and ECAR plots of Seahorse XFe96 runs with 3T3 and iMF fibroblasts, intracellular pyruvate levels and Ki67-positive cells in irradiated fibroblast populations, autophagy markers in 4T1 TNBC cells when incubated with control and irradiated fibroblast CM, and proliferative effects of AZD3965 on 4T1 TNBC cells.

Data Availability

All data needed to evaluate the conclusions in the paper are present in the article and supplemental material.

Disclosure of Potential Conflicts of Interest

The authors declare no competing financial interests.

Author Contributions

Conception and design: KC Corn, M Rafat
Development of methodology: KC Corn, M Rafat
Acquisition of data: KC Corn, LS Britto, YK Mohamed, YI Ivanova, T Zhu
Analysis and interpretation of data: KC Corn, LS Britto, YK Mohamed, YI Ivanova, T Zhu, M Rafat
Writing, review, and/or revision of the manuscript: KC Corn, M Rafat
Study supervision: M Rafat

Acknowledgments

The authors thank Dr. Christopher Contag for providing luciferase-labeled 4T1s, Dr. Charlotte Kuperwasser for providing immortalized reduction mammoplasty fibroblast cells, Dr. Craig Duvall for the use of the IVIS, and Dr. Michael Freeman for the use of the Cesium irradiator. The results shown here are in part based upon data generated by the TCGA Research Network: https://www.cancer.gov/tcga. We would also like to thank Dr. Rachelle Johnson for her guidance in accessing and analyzing TCGA BRCA data, and Dr. Alyssa Hasty for her critical review of our manuscript. Experiments using the Seahorse XFe96 Metabolic Flux Analyzer were performed in the Vanderbilt High-Throughput Screening Core Facility, which receives support from the Vanderbilt Institute of Chemical Biology and the Vanderbilt Ingram Cancer Center (P30 CA68485). This research was financially supported by NIH grant #R00CA201304, the American Cancer Society Research Scholar Grant, the Ruth L. Kirschstein National Research Service Award grant #T32DK101003 (KCC), and the Maximizing Access to Research Careers Award

grant #T34GM136451 (LSB). Schematics were prepared by the authors using BioRender.

References

Adra, J., D. Lundstedt, F. Killander, E. Holmberg, M. Haghanegi, E. Kjellén, P. Karlsson, and S. Alkner. 2019. Distribution of Locoregional Breast Cancer Recurrence in Relation to Postoperative Radiation Fields and Biological Subtypes. *Int. J. Radiat. Oncol.* 105:285–295. doi:10.1016/j.ijrobp.2019.06.013.

Auciello, F.R., V. Bulusu, C. Oon, J. Tait-Mulder, M. Berry, S. Bhattacharyya, S. Tumanov, B.L. Allen-Petersen, J. Link, N.D. Kendsersky, E. Vringer, M. Schug, D. Novo, R.F. Hwang, R.M. Evans, C. Nixon, C. Dorrell, J.P. Morton, J.C. Norman, R.C. Sears, J.J. Kamphorst, and M.H. Sherman. 2019. A Stromal Lysolipid–Autotaxin Signaling Axis Promotes Pancreatic Tumor Progression. *Cancer Discov.* 9:617–627. doi:10.1158/2159-8290.CD-18-1212.

Becker, L.M., J.T. O'Connell, A.P. Vo, M.P. Cain, D. Tampe, L. Bizarro, H. Sugimoto, A.K. McGow, J.M. Asara, S. Lovisa, K.M. McAndrews, R. Zielinski, P.L. Lorenzi, M. Zeisberg, S. Raza, V.S. LeBleu, and R. Kalluri. 2020. Epigenetic Reprogramming of Cancer-Associated Fibroblasts Deregulates Glucose Metabolism and Facilitates Progression of Breast Cancer. *Cell Rep.* 31:107701. doi:10.1016/J.CELREP.2020.107701.

Benyahia, Z., M.C.N.M. Blackman, L. Hamelin, L.X. Zampieri, T. Capeloa, M.L. Bedin, T. Vazeille, O. Schakman, and P. Sonveaux. 2021. In Vitro and In Vivo Characterization of MCT1 Inhibitor AZD3965 Confirms Preclinical Safety Compatible with Breast Cancer Treatment. *Cancers 2021, Vol. 13, Page 569*. 13:569. doi:10.3390/CANCERS13030569.

Chacko, B.K., P.A. Kramer, S. Ravi, G.A. Benavides, T. Mitchell, B.P. Dranka, D. Ferrick, A.K. Singal, S.W. Ballinger, S.M. Bailey, R.W. Hardy, J. Zhang, D. Zhi, and V.M. Darley-Usmar. 2014. The Bioenergetic Health Index: a new concept in mitochondrial translational research. *Clin. Sci.* 127:367–373. doi:10.1042/CS20140101.

Chuang, H.-Y., Y.-P. Lee, W.-C. Lin, Y.-H. Lin, and J.-J. Hwang. 2019. Fatty Acid Inhibition Sensitizes Androgen-Dependent and -Independent Prostate Cancer to Radiotherapy via FASN/NF-κB Pathway. *Sci. Rep.* 9. doi:10.1038/s41598-019-49486-2.

Corn, K.C., M.A. Windham, and M. Rafat. 2020. Lipids in the tumor microenvironment: From cancer progression to treatment. *Prog. Lipid Res.* 80:101055. doi:10.1016/j.plipres.2020.101055.

Darby, S., P. McGale, C. Correa, C. Taylor, R. Arriagada, M. Clarke, D. Cutter, C. Davies, M. Ewertz, J. Godwin, R. Gray, L. Pierce, T. Whelan, Y. Wang, R. Peto, K. Albain, S. Anderson, R. Arriagada, W. Barlow, J. Bergh, J. Bliss, M. Buyse, D. Cameron, E. Carrasco, M. Clarke, C. Correa, A. Coates, R. Collins, J. Costantino, D. Cutter, J. Cuzick, S. Darby,

N. Davidson, C. Davies, K. Davies, A. Delmestri, A. Di Leo, M. Dowsett, P. Elphinstone, V. Evans, M. Ewertz, R. Gelber, L. Gettins, C. Geyer, A. Goldhirsch, J. Godwin, R. Gray, C. Gregory, D. Hayes, C. Hill, J. Ingle, R. Jakesz, S. James, M. Kaufmann, A. Kerr, E. MacKinnon, P. McGale, T. McHugh, L. Norton, Y. Ohashi, S. Paik, H.C. Pan, E. Perez, M. Piccart, L. Pierce, K. Pritchard, G. Pruneri, V. Raina, P. Ravdin, J. Robertson, E. Rutgers, Y. F Shao, S. Swain, C. Taylor, P. Valagussa, G. Viale, T. Whelan, E. Winer, Y. Wang, and W. Wood. 2011. Effect of radiotherapy after breast-conserving surgery on 10-year recurrence and 15-year breast cancer death: Meta-analysis of individual patient data for 10 801 women in 17 randomised trials. *Lancet*. 378:1707–1716. doi:10.1016/S0140-6736(11)61629-2.

David Voduc, K., M.C.U. Cheang, S. Tyldesley, K. Gelmon, T.O. Nielsen, and H. Kennecke. 2010. Breast Cancer Subtypes and the Risk of Local and Regional Relapse. *J. Clin. Oncol.* 28:1684–1691. doi:10.1200/JCO.2009.24.9284.

Deng, H., A. Kan, N. Lyu, M. He, X. Huang, S. Qiao, S. Li, W. Lu, Q. Xie, H. Chen, J. Lai, Q. Chen, X. Jiang, S. Liu, Z. Zhang, and M. Zhao. 2021. Tumor-derived lactate inhibit the efficacy of lenvatinib through regulating PD-L1 expression on neutrophil in hepatocellular carcinoma. *J. Immunother. Cancer*. 9:2305. doi:10.1136/JITC-2020-002305.

Dheeraj, A., C. Agarwal, I.R. Schlaepfer, D. Raben, R. Singh, R. Agarwal, and G. Deep. 2018. A novel approach to target hypoxic cancer cells via combining β-oxidation inhibitor etomoxir with radiation. *Hypoxia*. 6:23–33. doi:10.2147/hp.s163115.

Dranka, B.P., B.G. Hill, and V.M. Darley-Usmar. 2010. Mitochondrial reserve capacity in endothelial cells: The impact of nitric oxide and reactive oxygen species. *Free Radic. Biol. Med.* 48:905–914. doi:10.1016/J.FREERADBIOMED.2010.01.015.

Draoui, N., and O. Feron. 2011. Lactate shuttles at a glance: from physiological paradigms to anti-cancer treatments. *Dis. Model. Mech.* 4:727–732. doi:10.1242/DMM.007724.

Du, Q., Z. Tan, F. Shi, M. Tang, L. Xie, L. Zhao, Y. Li, J. Hu, M. Zhou, A. Bode, | Xiangjian Luo, and Y. Cao. 2019. PGC1α/CEBPB/CPT1A axis promotes radiation resistance of nasopharyngeal carcinoma through activating fatty acid oxidation. *Cancer Sci.* 110:2050–2062. doi:10.1111/cas.14011.

Endo, K., Y. Katsuyama, N. Taira, M. Yoshioka, Y. Okano, and H. Masaki. 2020. Impairment of the autophagy system in repetitively UVA-irradiated fibroblasts. *Photodermatol. Photoimmunol. Photomed.* 36:111–117. doi:10.1111/phpp.12516.

Gao, F., C. Liu, J. Guo, W. Sun, L. Xian, D. Bai, H. Liu, Y. Cheng, B. Li, J. Cui, C. Zhang, and J. Cai. 2015. Radiation-driven lipid accumulation and dendritic cell dysfunction in cancer. *Sci.*

Rep. 5. doi:10.1038/srep09613.

Goldman, M.J., B. Craft, M. Hastie, K. Repečka, F. McDade, A. Kamath, A. Banerjee, Y. Luo, D. Rogers, A.N. Brooks, J. Zhu, and D. Haussler. 2020. Visualizing and interpreting cancer genomics data via the Xena platform. *Nat. Biotechnol. 2020 386*. 38:675–678. doi:10.1038/s41587-020-0546-8.

Göttgens, E.-L., C.N. van den Heuvel, M.C. de Jong, J.H. Kaanders, W.P. Leenders, M. Ansems, J. Bussink, and P.N. Span. 2019. ACLY (ATP Citrate Lyase) Mediates Radioresistance in Head and Neck Squamous Cell Carcinomas and is a Novel Predictive Radiotherapy Biomarker. *Cancers (Basel).* 11:1971. doi:10.3390/cancers11121971.

Hacker, B.C., E.J. Lin, D.C. Herman, A.M. Questell, S.E. Martello, R.J. Hedges, A.J. Walker, and M. Rafat. 2023. Irradiated Mammary Spheroids Elucidate Mechanisms of Macrophage-Mediated Breast Cancer Recurrence. *Cell. Mol. Bioeng.* 16:393–403. doi:10.1007/S12195-023-00775-X/FIGURES/4.

Han, S., R. Wei, X. Zhang, N. Jiang, M. Fan, J.H. Huang, B. Xie, L. Zhang, W. Miao, A.C.-P. Butler, M.A. Coleman, A.T. Vaughan, Y. Wang, H.-W. Chen, J. Liu, and J.J. Li. 2019. CPT1A/2-Mediated FAO Enhancement—A Metabolic Target in Radioresistant Breast Cancer. *Front. Oncol.* 9. doi:10.3389/fonc.2019.01201.

Havas, K.M., V. Milchevskaya, K. Radic, A. Alladin, E. Kafkia, M. Garcia, J. Stolte, B. Klaus, N. Rotmensz, T.J. Gibson, B. Burwinkel, A. Schneeweiss, G. Pruneri, K.R. Patil, R. Sotillo, and M. Jechlinger. 2017. Metabolic shifts in residual breast cancer drive tumor recurrence. *J. Clin. Invest.* 127:2091–2105. doi:10.1172/JCI89914.

Hill, B.G., G.A. Benavides, J.J.R. Lancaster, S. Ballinger, L. Dell'Italia, J. Zhang, and V.M. Darley-Usmar. 2012. Integration of cellular bioenergetics with mitochondrial quality control and autophagy. *Biol. Chem.* 393:1485. doi:10.1515/HSZ-2012-0198.

Huang, Y.H., P.M. Yang, Q.Y. Chuah, Y.J. Lee, Y.F. Hsieh, C.W. Peng, and S.J. Chiu. 2014. Autophagy promotes radiation-induced senescence but inhibits bystander effects in human breast cancer cells. *Autophagy*. 10:1212–1228. doi:10.4161/auto.28772.

Jwa, E., K.H. Shin, J.Y. Kim, Y.H. Park, S.Y. Jung, E.S. Lee, I.H. Park, K.S. Lee, J. Ro, Y.J. Kim, and T.H. Kim. 2016. Locoregional Recurrence by Tumor Biology in Breast Cancer Patients after Preoperative Chemotherapy and Breast Conservation Treatment. *Cancer Res. Treat.* 48:1363. doi:10.4143/CRT.2015.456.

Katayama, I., Y. Hotokezaka, T. Matsuyama, T. Sumi, and T. Nakamura. 2008. Ionizing Radiation Induces Macrophage Foam Cell Formation and Aggregation Through JNK-Dependent Activation of CD36 Scavenger Receptors. *Int. J. Radiat. Oncol. Biol. Phys.*

70:835–846. doi:10.1016/j.ijrobp.2007.10.058.

Kinner, A., W. Wu, C. Staudt, and G. Iliakis. 2008. Gamma-H2AX in recognition and signaling of DNA double-strand breaks in the context of chromatin. *Nucleic Acids Res.* 36:5678–5694. doi:10.1093/nar/gkn550.

Klionsky, D.J., K. Abdelmohsen, A. Abe, M. Joynal Abedin, H. Abeliovich, A. Acevedo Arozena, H. Adachi, C.M. Adams, P.D. Adams, K. Adeli, P.J. Adhihetty, S.G. Adler, G. Agam, R. Agarwal, M.K. Aghi, M. Agnello, P. Agostinis, P. V Aguilar, J. Aguirre-Ghiso, E.M. Airoldi, S. Ait-Si-Ali, T. Akematsu, E.T. Akporiaye, M. Al-Rubeai, G.M. Albaiceta, C. Albanese, D. Albani, M.L. Albert, J. Aldudo, H. Algül, M. Alirezaei, I. Alloza, A. Almasan, M. Almonte-Beceril, E.S. Alnemri, C. Alonso, N. Altan-Bonnet, D.C. Altieri, S. Alvarez, L. Alvarez-Erviti, S. Alves, G. Amadoro, A. Amano, C. Amantini, S. Ambrosio, I. Amelio, A.O. Amer, M. Amessou, A. Amon, Z. An, F.A. Anania, S.U. Andersen, U.P. Andley, C.K. Andreadi, N. Andrieu-Abadie, A. Anel, D.K. Ann, S. Anoopkumar-Dukie, M. Antonioli, H. Aoki, N. Apostolova, S. Aquila, K. Aquilano, K. Araki, E. Arama, A. Aranda, J. Araya, A. Arcaro, E. Arias, H. Arimoto, A.R. Ariosa, J.L. Armstrong, T. Arnould, I. Arsov, K. Asanuma, V. Askanas, E. Asselin, R. Atarashi, S.S. Atherton, J.D. Atkin, L.D. Attardi, P. Auberger, G. Auburger, L. Aurelian, R. Autelli, L. Avagliano, M. Laura Avantaggiati, L. Avrahami, S. Awale, N. Azad, T. Bachetti, J.M. Backer, D.-H. Bae, J. Bae, O.-N. Bae, S. Han Bae, E.H. Baehrecke, S.-H. Baek, et al. 2016. Guidelines for the use and interpretation of assays for monitoring autophagy (3rd edition). *Autophagy*. 12:1–222.

Koboldt, D.C., R.S. Fulton, M.D. McLellan, H. Schmidt, J. Kalicki-Veizer, J.F. McMichael, L.L. Fulton, D.J. Dooling, L. Ding, E.R. Mardis, R.K. Wilson, A. Ally, M. Balasundaram, Y.S.N. Butterfield, R. Carlsen, C. Carter, A. Chu, E. Chuah, H.J.E. Chun, R.J.N. Coope, N. Dhalla, R. Guin, C. Hirst, M. Hirst, R.A. Holt, D. Lee, H.I. Li, M. Mayo, R.A. Moore, A.J. Mungall, E. Pleasance, A.G. Robertson, J.E. Schein, A. Shafiei, P. Sipahimalani, J.R. Slobodan, D. Stoll, A. Tam, N. Thiessen, R.J. Varhol, N. Wye, T. Zeng, Y. Zhao, I. Birol, S.J.M. Jones, M.A. Marra, A.D. Cherniack, G. Saksena, R.C. Onofrio, N.H. Pho, S.L. Carter, S.E. Schumacher, B. Tabak, B. Hernandez, J. Gentry, H. Nguyen, A. Crenshaw, K. Ardlie, R. Beroukhim, W. Winckler, G. Getz, S.B. Gabriel, M. Meyerson, L. Chin, R. Kucherlapati, K.A. Hoadley, J.T. Auman, C. Fan, Y.J. Turman, Y. Shi, L. Li, M.D. Topal, X. He, H.H. Chao, A. Prat, G.O. Silva, M.D. Iglesia, W. Zhao, J. Usary, J.S. Berg, M. Adams, J. Booker, J. Wu, A. Gulabani, T. Bodenheimer, A.P. Hoyle, J. V. Simons, M.G. Soloway, L.E. Mose, S.R. Jefferys, S. Balu, J.S. Parker, D.N. Hayes, C.M. Perou, S. Malik, S. Mahurkar, H. Shen, D.J. Weisenberger, et al. 2012. Comprehensive molecular portraits of human breast

tumours. *Nature*. 490:61–70. doi:10.1038/nature11412.

Kosmacek, E.A., and R.E. Oberley-Deegan. 2020. Adipocytes protect fibroblasts from radiation-induced damage by adiponectin secretion. *Sci. Rep.* 10:1–12. doi:10.1038/s41598-020-69352-w.

Kuo, L.J., and L.-X. Yang. 2008. Gamma-H2AX - a novel biomarker for DNA double-strand breaks. *In Vivo (Brooklyn).* 22:305–9.

Liu, G., S. Feng, L. Jia, C. Wang, Y. Fu, and Y. Luo. 2018. Lung fibroblasts promote metastatic colonization through upregulation of stearoyl-CoA desaturase 1 in tumor cells. *Oncogene*. 37:1519–1533. doi:10.1038/s41388-017-0062-6.

Lowery, A.J., M.R. Kell, R.W. Glynn, M.J. Kerin, and K.J. Sweeney. 2012. Locoregional recurrence after breast cancer surgery: a systematic review by receptor phenotype. *Breast Cancer Res. Treat.* 133:831–841. doi:10.1007/s10549-011-1891-6.

Manoharan, I., P.D. Prasad, M. Thangaraju, and S. Manicassamy. 2021. Lactate-Dependent Regulation of Immune Responses by Dendritic Cells and Macrophages. *Front. Immunol.* 12:691134. doi:10.3389/FIMMU.2021.691134/BIBTEX.

Martinez-Outschoorn, U.E., M.P. Lisanti, and F. Sotgia. 2014. Catabolic cancer-associated fibroblasts transfer energy and biomass to anabolic cancer cells, fueling tumor growth. *Semin. Cancer Biol.* 25:47–60. doi:10.1016/J.SEMCANCER.2014.01.005.

Mauro-Lizcano, M., L. Esteban-Martínez, E. Seco, A. Serrano-Puebla, L. Garcia-Ledo, C. Figueiredo-Pereira, H.L.A. Vieira, and P. Boya. 2015. New method to assess mitophagy flux by flow cytometry. *Autophagy*. 11:833–843. doi:10.1080/15548627.2015.1034403/SUPPL_FILE/KAUP_A_1034403_SM1641.PDF.

Mizushima, N., T. Yoshimori, and B. Levine. 2010. Methods in Mammalian Autophagy Research. *Cell*. 140:313–326. doi:10.1016/J.CELL.2010.01.028.

Mu, X., W. Shi, Y. Xu, C. Xu, T. Zhao, B. Geng, J. Yang, J. Pan, S. Hu, C. Zhang, J. Zhang, C. Wang, J. Shen, Y. Che, Z. Liu, Y. Lv, H. Wen, and Q. You. 2018. Tumor-derived lactate induces M2 macrophage polarization via the activation of the ERK/STAT3 signaling pathway in breast cancer. *Cell Cycle*. 17:428–438. doi:10.1080/15384101.2018.1444305.

Neuwirt, H., J. Bouchal, G. Kharaishvili, C. Ploner, K. Jöhrer, F. Pitterl, A. Weber, H. Klocker, and I.E. Eder. 2020. Cancer-associated fibroblasts promote prostate tumor growth and progression through upregulation of cholesterol and steroid biosynthesis. *Cell Commun. Signal.* 18:11. doi:10.1186/s12964-019-0505-5.

Nguyen, T.B., S.M. Louie, J.R. Daniele, Q. Tran, A. Dillin, R. Zoncu, D.K. Nomura, and J.A. Olzmann. 2017. DGAT1-Dependent Lipid Droplet Biogenesis Protects Mitochondrial

Function during Starvation-Induced Autophagy. *Dev. Cell*. 42:9-21.e5. doi:10.1016/j.devcel.2017.06.003.

Noe, J.T., B.E. Rendon, A.E. Geller, L.R. Conroy, S.M. Morrissey, L.E.A. Young, R.C. Bruntz, E.J. Kim, A. Wise-Mitchell, M.B. De Souza Rizzo, E.R. Relich, B. V. Baby, L.A. Johnson, H.C. Affronti, K.M. McMasters, B.F. Clem, M.S. Gentry, J. Yan, K.E. Wellen, R.C. Sun, and R.A. Mitchell. 2021. Lactate supports a metabolic-epigenetic link in macrophage polarization. *Sci. Adv.* 7:8602. doi:10.1126/SCIADV.ABI8602/SUPPL_FILE/SCIADV.ABI8602_SM.PDF.

Qiu, B., and M.C. Simon. 2016. BODIPY 493/503 Staining of Neutral Lipid Droplets for Microscopy and Quantification by Flow Cytometry. *Bio-protocol*. 6. doi:10.21769/BIOPROTOC.1912.

Rafat, M., T.A. Aguilera, M. Vilalta, L.L. Bronsart, L.A. Soto, R. von Eyben, M.A. Golla, Y. Ahrari, S. Melemenidis, A. Afghahi, M.J. Jenkins, A.W. Kurian, K.C. Horst, A.J. Giaccia, and E.E. Graves. 2018. Macrophages Promote Circulating Tumor Cell–Mediated Local Recurrence following Radiotherapy in Immunosuppressed Patients. *Cancer Res.* 78:4241–4252. doi:10.1158/0008-5472.CAN-17-3623.

Rodemann, H.P., and M. Bamberg. 1995. Cellular basis of radiation-induced fibrosis. *Radiother. Oncol.* 35:83–90. doi:10.1016/0167-8140(95)01540-W.

Runwal, G., E. Stamatakou, F.H. Siddiqi, C. Puri, Y. Zhu, and D.C. Rubinsztein. 2019. LC3-positive structures are prominent in autophagy-deficient cells. *Sci. Rep.* 9:1–14. doi:10.1038/s41598-019-46657-z.

Sabbatinelli, J., F. Prattichizzo, F. Olivieri, A.D. Procopio, M.R. Rippo, and A. Giuliani. 2019. Where Metabolism Meets Senescence: Focus on Endothelial Cells. *Front. Physiol.* 10:1523. doi:10.3389/FPHYS.2019.01523/BIBTEX.

Santi, A., A. Caselli, F. Ranaldi, P. Paoli, C. Mugnaioni, E. Michelucci, and P. Cirri. 2015. Cancer associated fibroblasts transfer lipids and proteins to cancer cells through cargo vesicles supporting tumor growth. *Biochim. Biophys. Acta - Mol. Cell Res.* 1853:3211–3223. doi:10.1016/j.bbamcr.2015.09.013.

Sawyer, B.T., L. Qamar, T.M. Yamamoto, A. McMellen, Z.L. Watson, J.K. Richer, K. Behbakht, I.R. Schlaepfer, and B.G. Bitler. 2020. Targeting Fatty Acid Oxidation to Promote Anoikis and Inhibit Ovarian Cancer Progression. *Mol. cancer Res.* 18:1088–1098. doi:10.1158/1541-7786.MCR-19-1057.

Schindelin, J., I. Arganda-Carreras, E. Frise, V. Kaynig, M. Longair, T. Pietzsch, S. Preibisch, C. Rueden, S. Saalfeld, B. Schmid, J.Y. Tinevez, D.J. White, V. Hartenstein, K. Eliceiri, P.

Tomancak, and A. Cardona. 2012. Fiji: an open-source platform for biological-image analysis. *Nat. Methods 2012 97*. 9:676–682. doi:10.1038/nmeth.2019.

Sherry, A.D., R. von Eyben, N.B. Newman, P. Gutkin, I. Mayer, K. Horst, A.B. Chakravarthy, and M. Rafat. 2020. Systemic Inflammation After Radiation Predicts Locoregional Recurrence, Progression, and Mortality in Stage II-III Triple-Negative Breast Cancer. *Int. J. Radiat. Oncol. Biol. Phys.* 108:268–276. doi:10.1016/j.ijrobp.2019.11.398.

Siegel, R.L., K.D. Miller, N.S. Wagle, and A. Jemal. 2023. Cancer statistics, 2023. *CA. Cancer J. Clin.* 73:17–48. doi:10.3322/CAAC.21763.

Sioshansi, S., S. Ehdaivand, C. Cramer, M.M. Lomme, L.L. Price, and D.E. Wazer. 2012. Triple negative breast cancer is associated with an increased risk of residual invasive carcinoma after lumpectomy. *Cancer*. 118:3893–3898. doi:10.1002/cncr.27376.

Smith, B.D., J.R. Bellon, R. Blitzblau, G. Freedman, B. Haffty, C. Hahn, F. Halberg, K. Hoffman, K. Horst, J. Moran, C. Patton, J. Perlmutter, L. Warren, T. Whelan, J.L. Wright, and R. Jagsi. 2018. Radiation therapy for the whole breast: Executive summary of an American Society for Radiation Oncology (ASTRO) evidence-based guideline. *Pract. Radiat. Oncol.* 8:145–152. doi:10.1016/j.prro.2018.01.012.

Somwar, R., C.T. Roberts, and O. Varlamov. 2011. Live-cell imaging demonstrates rapid cargo exchange between lipid droplets in adipocytes. *FEBS Lett.* 585:1946–1950. doi:10.1016/j.febslet.2011.05.016.

Sung, H., J. Ferlay, R.L. Siegel, M. Laversanne, I. Soerjomataram, A. Jemal, and F. Bray. 2021. Global Cancer Statistics 2020: GLOBOCAN Estimates of Incidence and Mortality Worldwide for 36 Cancers in 185 Countries. *CA. Cancer J. Clin.* 71:209–249. doi:10.3322/caac.21660.

Sztalryd, C., and D.L. Brasaemle. 2017. The perilipin family of lipid droplet proteins: Gatekeepers of intracellular lipolysis. *Biochim. Biophys. Acta - Mol. Cell Biol. Lipids*. 1862:1221–1232. doi:10.1016/j.bbalip.2017.07.009.

Tan, Z., L. Xiao, M. Tang, J. Li, L. Li, F. Shi, N. Li, Y. Li, Q. Du, J. Lu, X. Weng, W. Yi, H. Zhang, J. Fan, J. Zhou, Q. Gao, J.N. Onuchic, A.M. Bode, X. Luo, and Y. Cao. 2018. Targeting CPT1A-mediated fatty acid oxidation sensitizes nasopharyngeal carcinoma to radiation therapy. *Theranostics*. 8:2329–2347. doi:10.7150/thno.21451.

Vilalta, M., M. Rafat, A.J. Giaccia, and E.E. Graves. 2014. Recruitment of Circulating Breast Cancer Cells Is Stimulated by Radiotherapy. *Cell Rep.* 8:402–409. doi:10.1016/J.CELREP.2014.06.011.

Wang, J., X. Wang, Y. Guo, L. Ye, D. Li, A. Hu, S. Cai, B. Yuan, S. Jin, Y. Zhou, Q. Li, L. Zheng,

and Q. Tong. 2021. Therapeutic targeting of SPIB/SPI1-facilitated interplay of cancer cells and neutrophils inhibits aerobic glycolysis and cancer progression. *Clin. Transl. Med.* 11:e588. doi:10.1002/CTM2.588.

Wang, X., J. Zhang, J. Fu, J. Wang, S. Ye, W. Liu, and C. Shao. 2015. Role of ROS-mediated autophagy in radiation-induced bystander effect of hepatoma cells. *Int. J. Radiat. Biol.* 91:452–458. doi:10.3109/09553002.2015.1012308.

Wang, Y. nan, Z. lei Zeng, J. Lu, Y. Wang, Z. xian Liu, M. ming He, Q. Zhao, Z. xian Wang, T. Li, Y. xin Lu, Q. nian Wu, K. Yu, F. Wang, H.Y. Pu, B. Li, W. Jia, M. Shi, D. Xie, T. bang Kang, P. Huang, H. qiang Ju, and R. hua Xu. 2018. CPT1A-mediated fatty acid oxidation promotes colorectal cancer cell metastasis by inhibiting anoikis. *Oncogene*. 37:6025–6040. doi:10.1038/s41388-018-0384-z.

Wapnir, I.L., and A. Khan. 2019. Current Strategies for the Management of Locoregional Breast Cancer Recurrence. *Oncol. (willist. Park.* 33:19–25.

Xiao, B., X. Deng, W. Zhou, and E.K. Tan. 2016. Flow cytometry-based assessment of mitophagy using mitotracker. *Front. Cell. Neurosci.* 10:1–4. doi:10.3389/FNCEL.2016.00076/BIBTEX.

Xu, S., F. Zou, Z. Diao, S. Zhang, Y. Deng, X. Zhu, L. Cui, J. Yu, Z. Zhang, A.T. Bamigbade, H. Zhang, X. Wei, X. Zhang, B. Liang, and P. Liu. 2019. Perilipin 2 and lipid droplets provide reciprocal stabilization. *Biophys. Reports*. 5:145–160. doi:10.1007/s41048-019-0091-5.

Zhang, C., S. Wang, H.P. Israel, S.X. Yan, D.P. Horowitz, S. Crockford, D. Gidea-Addeo, K.S. Clifford Chao, K. Kalinsky, and E.P. Connolly. 2015. Higher locoregional recurrence rate for triple-negative breast cancer following neoadjuvant chemotherapy, surgery and radiotherapy. *Springerplus*. 4:1–9. doi:10.1186/s40064-015-1116-2.

Zhao, X., P. Psarianos, L.S. Ghoraie, K. Yip, D. Goldstein, R. Gilbert, I. Witterick, H. Pang, A. Hussain, J.H. Lee, J. Williams, S. V. Bratman, L. Ailles, B. Haibe-Kains, and F.-F. Liu. 2019. Metabolic regulation of dermal fibroblasts contributes to skin extracellular matrix homeostasis and fibrosis. *Nat. Metab.* 1:147–157. doi:10.1038/s42255-018-0008-5.

Zorin, V., A. Zorina, N. Smetanina, P. Kopnin, I. V. Ozerov, S. Leonov, A. Isaev, D. Klokov, and A.N. Osipov. 2017. Diffuse colonies of human skin fibroblasts in relation to cellular senescence and proliferation. *Aging (Albany. NY).* 9:1404. doi:10.18632/AGING.101240.

Figure Legends

Figure 1. Radiation increases lipid droplets in fibroblasts. (A) Bioluminescence imaging signal of $4T1^{luc}$ TNBC cells co-cultured with either unirradiated or 6-day post-RT 3T3s for 48 hours normalized to signal from $4T1^{luc}$ TNBC cells alone (n = 5). **(B)** Kaplan-Meier analysis of overall survival utilizing NAT data from the TCGA BRCA dataset accessed through UCSC's Xena platform (Goldman et al., 2020; Koboldt et al., 2012) and grouping patients based on high or low *Plin2* gene expression. **(C)** Representative images of 3T3s stained with perilipin-2 (red) and counterstained with NucBlue (blue) at 7 days after RT. **(D)** Quantification of the cross-sectional area of lipid droplets from perilipin-2 IF staining of 3T3s (n = 5). **(E)** Representative images of 3T3s stained with ORO and counterstained with hematoxylin at 7 days after RT. **(F)** Quantification of the lipid droplet area positively stained with ORO in 3T3s and normalized per cell (n = 4, 3 day; n = 6, 7 day). **(G)** Representative images of human iMFs stained with ORO and counterstained with hematoxylin at 7 days after RT. **(H)** Quantification of the lipid droplet area positively stained with ORO in iMFs and normalized per cell (n = 3 – 4). For **A** and **D–H**, statistical significance was determined by an unpaired two-tailed t-test within timepoints with *$p<0.05$ and **$p<0.01$. For **B,** statistical analysis was performed using the log-rank test. Error bars show standard deviation. Scale bars are 50 µm.

Figure 2. Radiation induces prolonged autophagy upregulation in fibroblasts and promotes lipid droplet formation. **(A)** Representative images of 3T3s 3 days after RT following BODIPY-labeled palmitate (green) uptake. Cells are counterstained with Hoechst (blue). **(B)** Quantification of fluorescence images of BODIPY-labeled palmitate uptake in irradiated and control 3T3s up to 7 days after RT (n = 3). **(C)** Representative images of LysoTracker Red DND-99 staining (red) with NucBlue counterstaining (blue) in irradiated and control 3T3s 3 days after RT. **(D)** Quantification of live cell lysosomal staining in irradiated and control 3T3s (n = 4). **(E)** Representative images of LC3B staining (green) with NucBlue counterstaining (blue) 3 days after RT in 3T3s. Autophagosomes are identified by the formation of bright LC3B puncta. **(F)** Quantification of normalized autophagosome cross-sectional area per cell in irradiated and control 3T3s up to 7 days after RT (n = 5). **(G)** Representative images of LC3B staining (green) with NucBlue counterstaining (blue) in irradiated and unirradiated 3T3s 3 days after RT following autophagy inhibition with CQ. **(H)** Corresponding quantification of normalized autophagosome cross-sectional area per cell in irradiated and control 3T3s at 3 and 7 days after RT (n = 6, 3 day, non-equal variances; n = 5, 7 day, equal variances). **(I)** Quantification of the lipid droplet area positively stained with ORO in irradiated and control 3T3s

at 3 and 7 days after RT with and without CQ incubation (n = 4, equal variances). **(J)** Quantification of ORO staining in irradiated and control iMFs at 3 and 7 days after RT with and without CQ incubation (n = 3 – 4, equal variances). For **A**, **E**, and **G**, scale bars are 50 µm. For **C**, scale bars are 10 µm. For **B–F**, statistical analysis was determined by an unpaired two-tailed t-test within timepoints with *p<0.05, **p<0.01, and ***p<0.001. For **H–J**, Statistical analysis was determined by one-way ANOVA with Tukey simultaneous tests for equal variances or Games-Howell pairwise comparisons for non-equal variances with *p<0.05 and **p<0.01. Error bars show standard deviation.

Figure 3. Radiation-induced autophagy maintains high levels of mitochondrial respiration and aerobic glycolysis following damage. (A) Representative flow cytometry analysis of MitoTracker-Deep-Red-stained irradiated and unirradiated 3T3s at 3 and 7 days after RT. **(B)** Representative flow cytometry analysis of MitoTracker-Deep-Red-stained irradiated and unirradiated 3T3s with and without CQ incubation. **(C)** ATP-linked OCR in irradiated and unirradiated 3T3s with and without CQ incubation (n = 3 biological replicates, non-equal variances). **(D)** Non-mitochondrial OCR in irradiated and unirradiated 3T3s at 3 and 7 days after RT (n = 3 biological replicates). **(E)** ATP-linked OCR in irradiated and unirradiated 3T3s at 3 and 7 days after RT with and without etomoxir incubation to evaluate FAO (n = 3 biological replicates; non-equal variances for 3 day timepoint and equal variances for 7 day timepoint). **(F)** Baseline ECAR in irradiated and unirradiated 3T3s at 3 and 7 days after RT with and without CQ incubation (n = 3 biological replicates, equal variances). **(G)** Glycolytic ECAR in irradiated and unirradiated 3T3s 7 days after RT with and without CQ incubation (n = 3 biological replicates, non-equal variances). **(H)** Reserve glycolytic ECAR in irradiated and unirradiated 3T3s 7 days after RT with and without CQ incubation (n = 3 biological replicates, equal variances). **(I)** Glycolytic ECAR in irradiated and unirradiated iMFs 7 days after RT with and without CQ incubation (n = 3 biological replicates, non-equal variances). **(J)** ATP-linked OCR in irradiated and unirradiated iMFs 7 days after RT with and without CQ incubation (n = 3 biological replicates, non-equal variances). Statistical analyses for **A–C** and **E–J** determined by one-way ANOVA using either Tukey or Games-Howell pairwise comparison corrections for equal or non-equal variances, respectively. Symbols for pairwise comparisons: * for comparison to 0 Gy & 0 µM inhibitor, # for comparison to 10 Gy & 0 µM inhibitor, and + for comparison to 0 Gy & high concentration of inhibitor, where $^{*,\#,+}$p<0.05, $^{**,\#\#,++}$p<0.01, and $^{***,\#\#\#,+++}$p<0.001. Statistical analysis for **D** was determined by an unpaired two-tailed t-test with ***p<0.001. Error bars show standard deviation.

Figure 4. Radiation-induced aerobic glycolysis of fibroblasts results in lactate metabolic crosstalk with breast cancer cells. (A) Quantification of live cell lysosomal staining in 4T1s incubated with 7-day post-RT or unirradiated control 3T3 fibroblast CM (n = 3). **(B)** Normalized autophagosome cross-sectional area per cell in TNBC cells incubated with 7-day post-RT or unirradiated 3T3 fibroblast CM (n = 5). **(C)** Quantification of L-lactate concentration in fibroblast CM collected 7 days after RT from irradiated and unirradiated 3T3s (n = 4). **(D)** Representative images of 4T1 cells in scratch wound assays at 0-, 6-, and 15-hour timepoints following incubation in either 7-day post-RT or unirradiated fibroblast CM. Scale bars are 200 µm. **(E)** Quantification of the percent closure of the scratch wound gap of 4T1 cells 15-hours following gap creation (n = 5 – 6). **(F)** Representative images of 4T1 TNBC tumor spheroids after 9 days of incubation in either 7-day post-RT or unirradiated fibroblast CM with or without 50 nM AZD3965. Scale bars are 500 µm. **(G)** Quantification of the percent outgrowth from the core of tumor spheroids at 9 days after incubation in fibroblast CM with or without AZD3965 (n = 5 biological replicates). **(H)** *Plin2* expression in NAT gathered from the TCGA BRCA dataset (Goldman et al., 2020) plotted against *Map1lc3b*, *Lipa*, and *Ldha* gene expression data with Pearson correlation coefficients (n = 113 patient samples). For **A, C,** and **E,** statistical analysis was determined by an unpaired two-tailed t-test with *$p<0.05$. For **B** and **G**, statistical analysis was determined by a Mann-Whitney non-parametric test for non-normally distributed distributions. For **B**, ***$p<0.001$. For **G,** **$p<0.01$ and ***$p<0.001$ shows statistical significance in comparison to 0 Gy + 0 nM AZD3965, $^{###}p<0.001$ in comparison to 10 Gy + 0 nM AZD3965, and $^{++}p<0.01$ in comparison to 0 Gy + 50 nM AZD3965. Error bars show standard deviation.

Figures

Figure 1

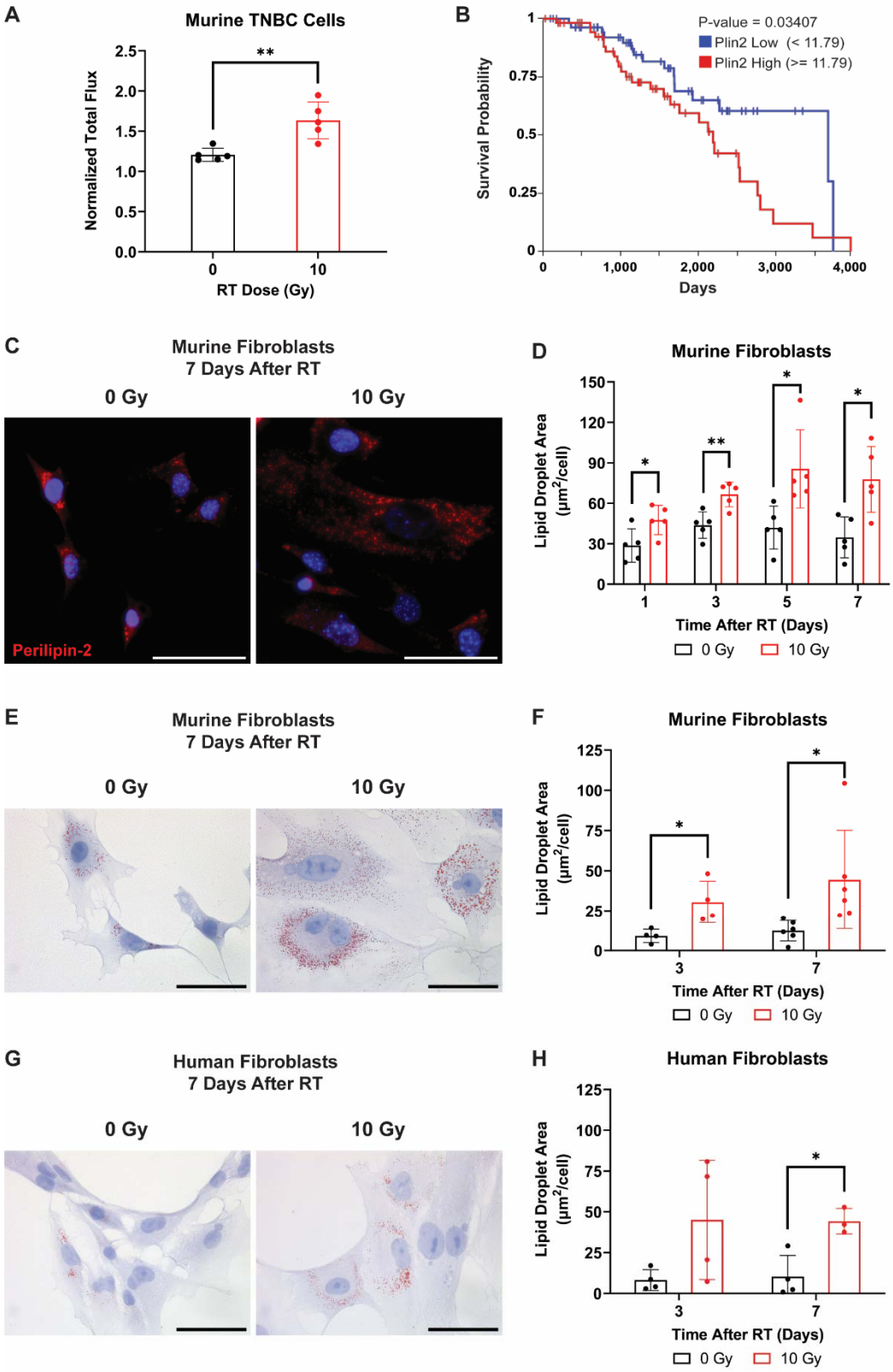

Figure 2

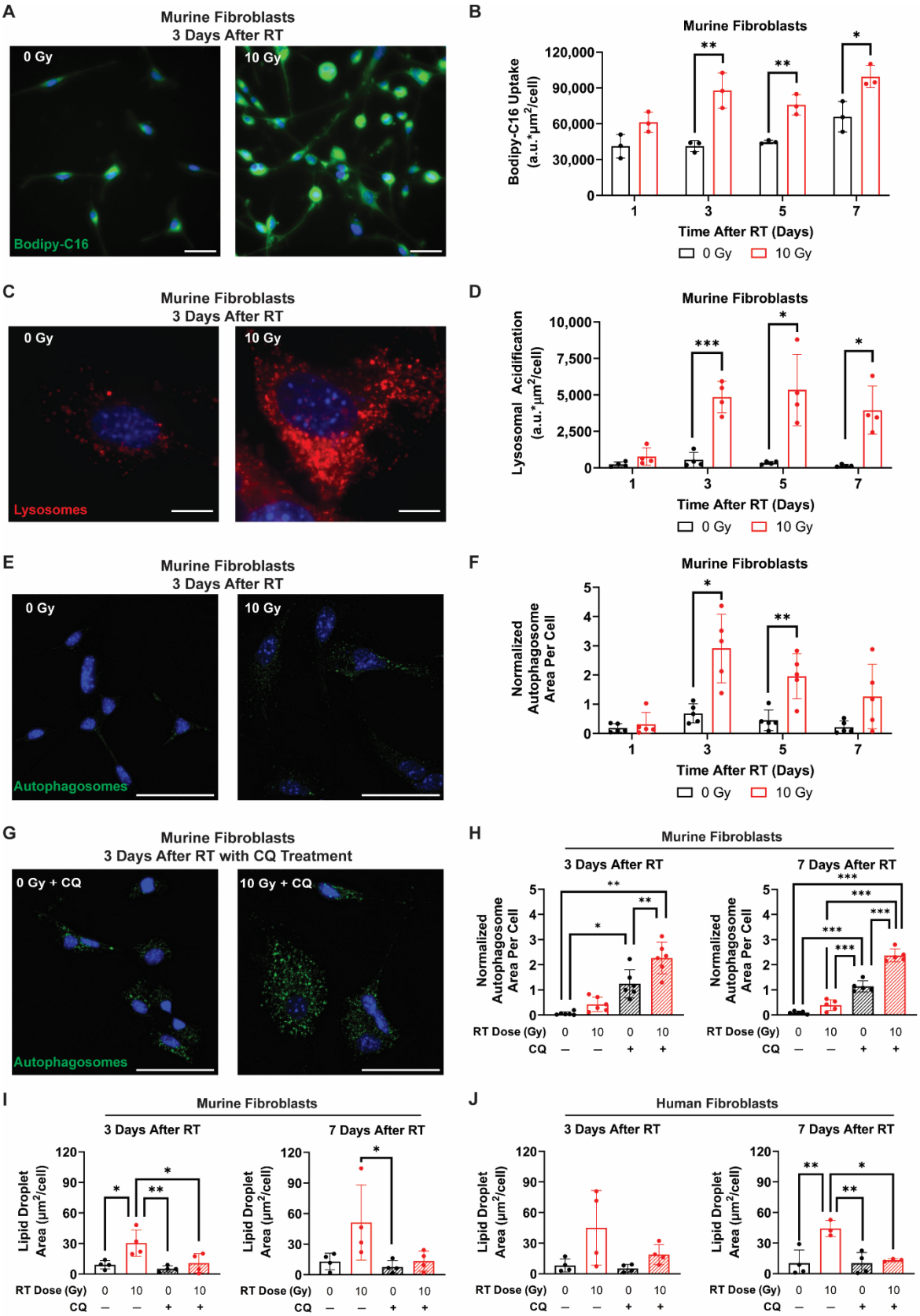
A
Murine Fibroblasts
3 Days After RT
0 Gy
10 Gy
Bodipy-C16
B
Murine Fibroblasts
Bodipy-C16 Uptake (a.u.*µm²/cell)
120,000
90,000
60,000
30,000
0
1
3
5
7
Time After RT (Days)
0 Gy
10 Gy
C
Murine Fibroblasts
3 Days After RT
0 Gy
10 Gy
Lysosomes
D
Murine Fibroblasts
Lysosomal Acidification (a.u.*µm²/cell)
10,000
7,500
5,000
2,500
0
Time After RT (Days)
0 Gy
10 Gy
E
Murine Fibroblasts
3 Days After RT
0 Gy
10 Gy
Autophagosomes
F
Murine Fibroblasts
Normalized Autophagosome Area Per Cell
Time After RT (Days)
0 Gy
10 Gy
G
Murine Fibroblasts
3 Days After RT with CQ Treatment
0 Gy + CQ
10 Gy + CQ
Autophagosomes
H
Murine Fibroblasts
3 Days After RT
7 Days After RT
Normalized Autophagosome Area Per Cell
RT Dose (Gy) 0 10 0 10
CQ – – + +
I
Murine Fibroblasts
3 Days After RT
7 Days After RT
Lipid Droplet Area (µm²/cell)
RT Dose (Gy) 0 10 0 10
CQ – – + +
J
Human Fibroblasts
3 Days After RT
7 Days After RT
Lipid Droplet Area (µm²/cell)
RT Dose (Gy) 0 10 0 10
CQ – – + +

Figure 3

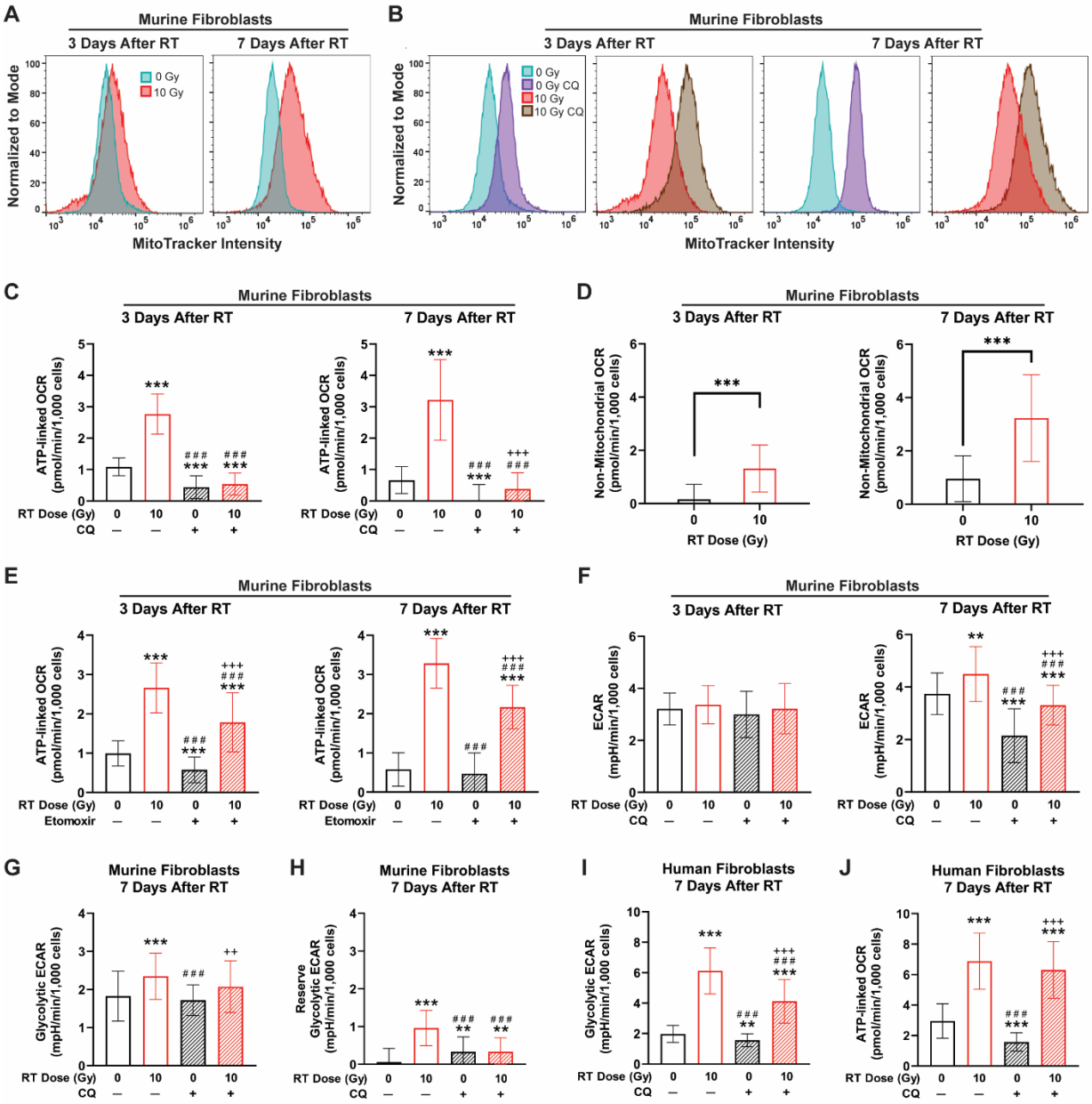
A
Murine Fibroblasts
3 Days After RT
7 Days After RT
Normalized to Mode
0 Gy
10 Gy
MitoTracker Intensity
B
Murine Fibroblasts
3 Days After RT
7 Days After RT
Normalized to Mode
0 Gy
0 Gy CQ
10 Gy
10 Gy CQ
MitoTracker Intensity
C
Murine Fibroblasts
3 Days After RT
7 Days After RT
ATP-linked OCR (pmol/min/1,000 cells)
RT Dose (Gy)
CQ
D
Murine Fibroblasts
3 Days After RT
7 Days After RT
Non-Mitochondrial OCR (pmol/min/1,000 cells)
RT Dose (Gy)
E
Murine Fibroblasts
3 Days After RT
7 Days After RT
ATP-linked OCR (pmol/min/1,000 cells)
RT Dose (Gy)
Etomoxir
F
Murine Fibroblasts
3 Days After RT
7 Days After RT
ECAR (mpH/min/1,000 cells)
RT Dose (Gy)
CQ
G
Murine Fibroblasts
7 Days After RT
Glycolytic ECAR (mpH/min/1,000 cells)
RT Dose (Gy)
CQ
H
Murine Fibroblasts
7 Days After RT
Reserve Glycolytic ECAR (mpH/min/1,000 cells)
RT Dose (Gy)
CQ
I
Human Fibroblasts
7 Days After RT
Glycolytic ECAR (mpH/min/1,000 cells)
RT Dose (Gy)
CQ
J
Human Fibroblasts
7 Days After RT
ATP-linked OCR (pmol/min/1,000 cells)
RT Dose (Gy)
CQ

Figure 4

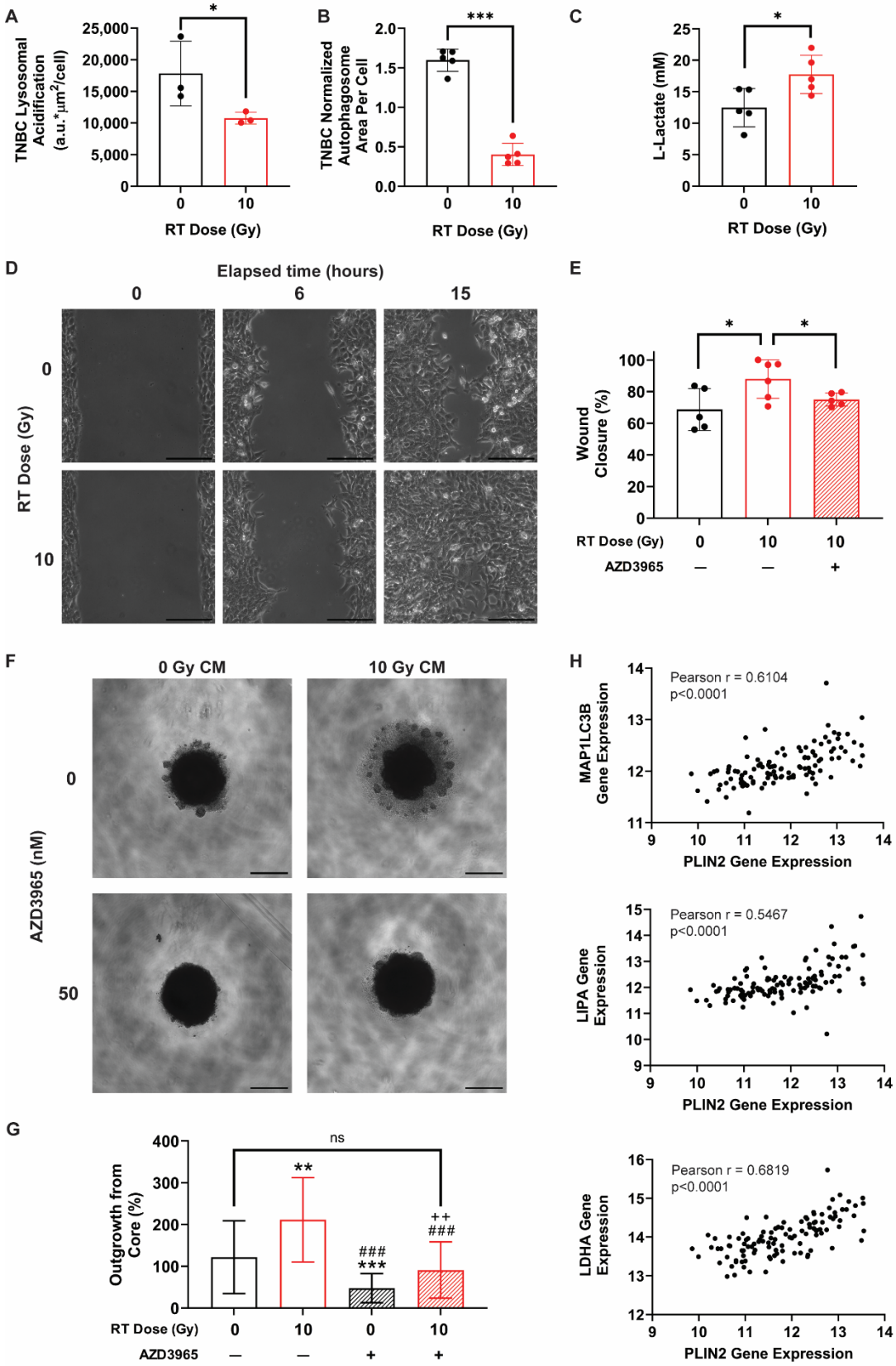
A
TNBC Lysosomal Acidification (a.u.*µm²/cell)
25,000
20,000
15,000
10,000
5,000
0
*
0
10
RT Dose (Gy)
B
TNBC Normalized Autophagosome Area Per Cell
2.0
1.5
1.0
0.5
0.0
***
0
10
RT Dose (Gy)
C
L-Lactate (mM)
25
20
15
10
5
0
*
0
10
RT Dose (Gy)
D
Elapsed time (hours)
0
6
15
RT Dose (Gy)
0
10
E
Wound Closure (%)
100
80
60
40
20
0
*
*
RT Dose (Gy) 0 10 10
AZD3965 — — +
F
0 Gy CM
10 Gy CM
AZD3965 (nM)
0
50
G
Outgrowth from Core (%)
400
300
200
100
0
ns
**
###
***
++
###
RT Dose (Gy) 0 10 0 10
AZD3965 — — + +
H
MAP1LC3B Gene Expression
Pearson r = 0.6104
p<0.0001
PLIN2 Gene Expression
LIPA Gene Expression
Pearson r = 0.5467
p<0.0001
PLIN2 Gene Expression
LDHA Gene Expression
Pearson r = 0.6819
p<0.0001
PLIN2 Gene Expression